

AD-A230 547

DTIC FILE COPY

①



DESIGN OF A LINEAR QUADRATIC
GAUSSIAN CONTROL LAW FOR AN
ADAPTIVE OPTICS SYSTEM

THESIS

Mark Alan Von Bokern
Captain, USAF

DEPARTMENT OF THE AIR FORCE
AIR UNIVERSITY

AIR FORCE INSTITUTE OF TECHNOLOGY

Wright-Patterson Air Force Base, Ohio

91 1 3 154

1

AFIT/GE/ENG/90D-65

DTIC
ELECTE
JAN 07 1991
S D

DESIGN OF A LINEAR QUADRATIC
GAUSSIAN CONTROL LAW FOR AN
ADAPTIVE OPTICS SYSTEM

THESIS

Mark Alan Von Bokern
Captain, USAF

AFIT/GE/ENG/90D-65

Approved for public release; distribution unlimited

AFIT/GE/ENG/90D-65

DESIGN OF A LINEAR QUADRATIC GAUSSIAN CONTROL LAW FOR AN
ADAPTIVE OPTICS SYSTEM

THESIS

Presented to the Faculty of the School of Engineering
of the Air Force Institute of Technology
Air University
In Partial Fulfillment of the
Requirements for the Degree of
Master of Science in Electrical Engineering

Mark Alan Von Bokern, B.S.
Captain, USAF

December, 1990

Approved for public release; distribution unlimited

REPORT DOCUMENTATION PAGE

Form Approved
GSA GEN. REG. NO. 27

1. AGENCY USE ONLY (Leave blank)

2. REPORT DATE
December 1990

3. REPORT TYPE AND DATES COVERED
Master's Thesis

4. TITLE AND SUBTITLE

DESIGN OF A LINEAR QUADRATIC GAUSSIAN CONTROL LAW
FOR AN ADAPTIVE OPTICS SYSTEM

5. FUNDING NUMBERS

6. AUTHOR(S)

Mark A. Von Bokern, Captain, USAF

7. PERFORMING ORGANIZATION NAME(S) AND ADDRESS(ES)

Air Force Institute of Technology, WPAFB OH 45433-6583

8. PERFORMING ORGANIZATION
REPORT NUMBER

AFIT/GE/ENG/90D-65

9. SPONSORING/MONITORING AGENCY NAME(S) AND ADDRESS(ES)

10. SPONSORING/MONITORING
AGENCY REPORT NUMBER

11. SUPPLEMENTARY NOTES

12. DISTRIBUTION/AVAILABILITY STATEMENT

Approved for public release; distribution unlimited

12b. DISTRIBUTION CODE

13. ABSTRACT (Maximum 200 words)

This thesis considers the design of a linear quadratic Gaussian (LQG) controller for a ground-based adaptive-optics telescope. The incoming aberrated image is reflected from a 97-element piezoelectric mirror, then measured with a Hartmann-type wavefront sensor. A Kalman filter processes the outputs of the wavefront sensor and obtains estimates of system states. A linear quadratic regulator processes these state estimates and determines an appropriate set of commands for the deformable mirror.

Atmospheric distortion is modeled as a set of fourteen Zernike coefficients whose dynamic behavior is produced by excitation of a set of shaping filters by zero-mean Gaussian white noise. The response of the mirror to control voltages is modeled as a set of Zernike coefficients whose dynamics are modeled as deterministic first-order systems. The entire control system is simulated using the Multimode Simulation for Optimal Filter Evaluation (MSOFE) software.

14. SUBJECT TERMS

Adaptive Optics, Automatic Control, Telescopes, Image Processing

15. NUMBER OF PAGES

179
16. PRICE CODE

17. SECURITY CLASSIFICATION
OF REPORT
Unclassified

18. SECURITY CLASSIFICATION
OF THIS PAGE
Unclassified

19. SECURITY CLASSIFICATION
OF ABSTRACT
Unclassified

20. LIMITATION OF ABSTRACT
UL

Vita

Captain Mark Alan Von Bokern was born on November 29th, 1959, in Covington, Kentucky. Graduating from Boone County High School, he attended Rose-Hulman Institute of Technology in Terre Haute, Indiana where he obtained the Bachelor of Science degree in Chemical Engineering. After a two-year assignment with Procter and Gamble Company in Cincinnati, he enrolled in Officer Training School where he received his commission in May of 1984. Second Lieutenant Von Bokern then attended Ohio University, receiving the Bachelor of Science degree in Electrical Engineering. Following a three-year tour at the Foreign Technology Division (AFSC), Wright-Patterson Air Force Base, he was assigned to the Air Force Institute of Technology for a Masters Degree in Electrical Engineering.

Permanent address: 50 Utz Drive
Florence, Kentucky 41042

Preface

This research develops a proof-of-concept design of a linear quadratic Gaussian controller for a phase-correcting, adaptive optics telescope. The dynamics and measurement models embedded in the controller are based for the most part on theoretical results from the literature. The correlation between these relationships and reality would of course directly affect performance of a fielded system. As Keats wrote, "truth is beauty."

The bulk of my thanks go to my thesis advisor, Capt Randy Paschall. He provided the optimum balance of initial (as opposed to inertial) guidance and terminal freedom. I'd also like to acknowledge assistance received from thesis committee members Capt Byron Welsh (optics) and Dr Peter Maybeck (stochastic control). Capts Mike Roggemann and Chuck Matson of the Air Force Weapons Lab provided additional encouragement and insight.

Finally my most deserved thanks go to my wife, Michelle, and to my three sons Joseph, Jonathan, and Jordan. The next college degrees will have their names on them.

Mark Alan Von Bokern

| | |
|--------------------|--------------------------|
| Accession For | |
| NTIS CRA&I | J |
| DTIC TAB | |
| Unannounced | |
| Justification | |
| By | |
| Distribution / | |
| Availability Codes | |
| Dist | Avail. and/or Special |
| A-1 | |



Table of Contents

| | Page |
|---|-------|
| Preface | ii |
| Table of Contents | iii |
| List of Figures | vii |
| List of Tables | xiv |
| List of Symbols | xv |
| Abstract | xviii |
| I. Introduction | 1-1 |
| 1.1 Motivation | 1-1 |
| 1.2 Research Objective | 1-2 |
| 1.3 Assumptions | 1-3 |
| 1.4 Treatment | 1-4 |
| II. Background | 2-1 |
| 2.1 Atmospheric Optics | 2-1 |
| 2.1.1 Introduction | 2-1 |
| 2.1.2 Turbulence | 2-1 |
| 2.1.3 Structure Functions | 2-2 |
| 2.1.4 Kolmogorov Statistics | 2-4 |
| 2.2 Zernike Functions | 2-8 |
| 2.2.1 Introduction | 2-8 |
| 2.2.2 Zernike Functions | 2-10 |
| 2.3 Stochastic State-Space Modeling | 2-15 |

| | Page |
|--|------|
| 2.4 Linear Quadratic Regulator | 2-18 |
| 2.4.1 Kalman Filter | 2-19 |
| 2.4.2 Linear Quadratic Regulation | 2-21 |
| 2.5 Summary | 2-22 |
| III. Stochastic Models | 3-1 |
| 3.1 Adaptive Optics System | 3-1 |
| 3.2 Atmospheric Effects | 3-1 |
| 3.3 Mirror | 3-4 |
| 3.3.1 Steady-State Mirror Behavior | 3-7 |
| 3.3.2 Transient Behavior | 3-13 |
| 3.4 Augmented System Dynamics | 3-19 |
| 3.5 Wavefront Sensor | 3-20 |
| 3.5.1 Wavefront Sensor Description | 3-20 |
| 3.5.2 Derivation of H' | 3-21 |
| 3.5.3 Derivation of R | 3-26 |
| 3.6 Summary | 3-27 |
| IV. Controller Design | 4-1 |
| 4.1 Kalman Filter Design | 4-1 |
| 4.2 Linear Quadratic Regulator Design | 4-4 |
| 4.3 Summary | 4-7 |
| V. Simulation Results | 5-1 |
| 5.1 Methodology | 5-1 |
| 5.2 Study 1 Description | 5-2 |
| 5.2.1 Simulated Atmospheric State Behavior | 5-3 |
| 5.2.2 Performance Analysis | 5-5 |
| 5.3 Performance Results | 5-10 |
| 5.4 Summary | 5-12 |

| | Page |
|---|------|
| VI. Conclusions and Recommendations | 6-1 |
| 6.1 Summary | 6-1 |
| 6.2 Conclusions | 6-1 |
| 6.3 Recommendations | 6-2 |
| 6.3.1 Modeling | 6-2 |
| 6.3.2 Adaptivity | 6-4 |
| 6.3.3 Time Delay | 6-5 |
| 6.3.4 Simplifications | 6-5 |
| Appendix A. Plots of Zernike Functions | A-1 |
| Appendix B. Justification of 15 Zernike Modes | B-1 |
| B.1 Mean Square Considerations | B-1 |
| B.2 Nyquist Considerations | B-3 |
| Appendix C. RMS Phase Error | C-1 |
| Appendix D. Determination of Atmospheric Distortion Shaping Filters . . | D-1 |
| D.1 Introduction | D-1 |
| D.2 Example | D-3 |
| D.3 Model | D-6 |
| D.4 Program | D-7 |
| Appendix E. Steady-State Influence Matrix | E-1 |
| Appendix F. Generation of Hartman Sensor Gain, N | F-1 |
| Appendix G. Plots of Atmospheric Distortion States, Study 1 | G-1 |
| G.1 State 1 | G-2 |
| G.2 State 2 | G-3 |
| G.3 State 3 | G-4 |

| | Page |
|---|--------|
| G.4 State 4 | G-5 |
| G.5 State 5 | G-6 |
| G.6 State 6 | G-7 |
| G.7 State 7 | G-8 |
| G.8 State 7 | G-9 |
| G.9 State 9 | G-10 |
| G.10 State 10 | G-11 |
| G.11 State 11 | G-12 |
| G.12 State 12 | G-13 |
| G.13 State 13 | G-14 |
| G.14 State 14 | G-15 |
| Appendix H. Plots From Studies One Through Nine | H-1 |
| H.1 Study 1 | H-2 |
| H.2 Study 2 | H-5 |
| H.3 Study 3 | H-8 |
| H.4 Study 4 | H-11 |
| H.5 Study 5 | H-14 |
| H.6 Study 6 | H-17 |
| H.7 Study 7 | H-20 |
| H.8 Study 8 | H-23 |
| H.9 Study 9 | H-26 |
| Bibliography | BIB-1 |
| Vita | VITA-1 |

List of Figures

| Figure | Page |
|---|------|
| 2.1. Refractive Index Structure Constant | 2-5 |
| 2.2. Planar Wavefronts at an Aperture | 2-8 |
| 2.3. Distorted Wavefronts at an Aperture | 2-9 |
| 2.4. Weighted Sum of Zernike Functions 0-14 | 2-14 |
| 2.5. Weighted Sum of Zernike Functions 1-14 | 2-15 |
| 2.6. Change in Radius | 2-16 |
| 2.7. Block Diagram of LQG Controller | 2-19 |
| 3.1. Simple Schematic of Adaptive Optics LQG Control | 3-2 |
| 3.2. Actuator Locations on Itek 97-Actuator Mirror | 3-5 |
| 3.3. Sketch of Actuator Displacement Linearity | 3-7 |
| 3.4. X-Axis Slice of Actuator #49 Influence Function | 3-9 |
| 3.5. Approximate Influence Function for Actuator #49 | 3-10 |
| 3.6. Simulated Mirror Reconstruction of 14-th Zernike Mode Phase Distortion | 3-13 |
| 3.7. Frequency Response of An AFWL Mirror Actuator Channel | 3-14 |
| 3.8. Subaperture Locations on Hartmann Wavefront Sensor | 3-21 |
| 3.9. Concept of Operation for Two-Dimensional Hartmann Sensor | 3-22 |
| 3.10. Slope Measurement Weighting Function | 3-24 |
| 5.1. Atmospheric Y-tilt State and Filter Estimate | 5-3 |
| 5.2. Atmospheric Y-tilt Filter Error and Filter Variance | 5-4 |
| 5.3. Mean and Standard Deviation of Atmospheric Y-tilt Filter Error | 5-6 |
| 5.4. RMS Phase Distortion Before and After Correction | 5-8 |
| 5.5. Monte Carlo Study of RMS Phase Distortion Before and After Correction | 5-8 |
| 5.6. Control Voltage Envelope for Monte Carlo Study | 5-9 |

| Figure | Page |
|--|------|
| 5.7. Monte Carlo Study of RMS Phase Distortion Caused by Filter Error . . . | 5-10 |
| A.1. Zernike Function 0 | A-1 |
| A.2. Zernike Function 1 | A-1 |
| A.3. Zernike Function 2 | A-2 |
| A.4. Zernike Function 3 | A-2 |
| A.5. Zernike Function 4 | A-2 |
| A.6. Zernike Function 5 | A-3 |
| A.7. Zernike Function 6 | A-3 |
| A.8. Zernike Function 7 | A-3 |
| A.9. Zernike Function 8 | A-4 |
| A.10. Zernike Function 9 | A-4 |
| A.11. Zernike Function 10 | A-4 |
| A.12. Zernike Function 11 | A-5 |
| A.13. Zernike Function 12 | A-5 |
| A.14. Zernike Function 13 | A-5 |
| A.15. Zernike Function 14 | A-6 |
| B.1. Relative Distortion with N Zernike Modes Removed | B-2 |
| B.2. Relative Distortion in the Incident Light with N Zernike Modes Removed | B-3 |
| D.1. Autocorrelation Data from ACOVAR2 Program | D-3 |
| D.2. Autocorrelation Data from ACOVAR2 Program and Fitted Curve . . . | D-5 |
| G.1. State 1 and Filter Estimate, Study 1 | G-2 |
| G.2. State 1 Filter Estimation Error and Filter Uncertainty, Study 1 | G-2 |
| G.3. State 1 Monte Carlo Study of Filter Error, Study 1 | G-2 |
| G.4. State 2 and Filter Estimate, Study 1 | G-3 |
| G.5. State 2 Filter Estimation Error and Filter Uncertainty, Study 1 | G-3 |
| G.6. State 2 Monte Carlo Study of Filter Error, Study 1 | G-3 |

| Figure | Page |
|--|------|
| G.7. State 3 and Filter Estimate, Study 1 | G-4 |
| G.8. State 3 Filter Estimation Error and Filter Uncertainty, Study 1 | G-4 |
| G.9. State 3 Monte Carlo Study of Filter Error, Study 1 | G-4 |
| G.10. State 4 and Filter Estimate, Study 1 | G-5 |
| G.11. State 4 Filter Estimation Error and Filter Uncertainty, Study 1 | G-5 |
| G.12. State 4 Monte Carlo Study of Filter Error, Study 1 | G-5 |
| G.13. State 5 and Filter Estimate, Study 1 | G-6 |
| G.14. State 5 Filter Estimation Error and Filter Uncertainty, Study 1 | G-6 |
| G.15. State 5 Monte Carlo Study of Filter Error, Study 1 | G-6 |
| G.16. State 6 and Filter Estimate, Study 1 | G-7 |
| G.17. State 6 Filter Estimation Error and Filter Uncertainty, Study 1 | G-7 |
| G.18. State 6 Monte Carlo Study of Filter Error, Study 1 | G-7 |
| G.19. State 7 and Filter Estimate, Study 1 | G-8 |
| G.20. State 7 Filter Estimation Error and Filter Uncertainty, Study 1 | G-8 |
| G.21. State 7 Monte Carlo Study of Filter Error, Study 1 | G-8 |
| G.22. State 8 and Filter Estimate, Study 1 | G-9 |
| G.23. State 8 Filter Estimation Error and Filter Uncertainty, Study 1 | G-9 |
| G.24. State 8 Monte Carlo Study of Filter Error, Study 1 | G-9 |
| G.25. State 9 and Filter Estimate, Study 1 | G-10 |
| G.26. State 9 Filter Estimation Error and Filter Uncertainty, Study 1 | G-10 |
| G.27. State 9 Monte Carlo Study of Filter Error, Study 1 | G-10 |
| G.28. State 10 and Filter Estimate, Study 1 | G-11 |
| G.29. State 10 Filter Estimation Error and Filter Uncertainty, Study 1 | G-11 |
| G.30. State 10 Monte Carlo Study of Filter Error, Study 1 | G-11 |
| G.31. State 11 and Filter Estimate, Study 1 | G-12 |
| G.32. State 11 Filter Estimation Error and Filter Uncertainty, Study 1 | G-12 |
| G.33. State 11 Monte Carlo Study of Filter Error, Study 1 | G-12 |

| Figure | Page |
|--|------|
| G.34. State 12 and Filter Estimate, Study 1 | G-13 |
| G.35. State 12 Filter Estimation Error and Filter Uncertainty, Study 1 | G-13 |
| G.36. State 12 Monte Carlo Study of Filter Error, Study 1 | G-13 |
| G.37. State 13 and Filter Estimate, Study 1 | G-14 |
| G.38. State 13 Filter Estimation Error and Filter Uncertainty, Study 1 | G-14 |
| G.39. State 13 Monte Carlo Study of Filter Error, Study 1 | G-14 |
| G.40. State 14 and Filter Estimate, Study 1 | G-15 |
| G.41. State 14 Filter Estimation Error and Filter Uncertainty, Study 1 | G-15 |
| G.42. State 14 Monte Carlo Study of Filter Error, Study 1 | G-15 |
| | |
| H.1. State 1 and Filter Estimate for Study 1 | H-2 |
| H.2. State 1 Filter Estimation Error and Filter Uncertainty for Study 1 . . . | H-2 |
| H.3. State 1 Monte Carlo Study of Filter Error for Study 1 | H-2 |
| H.4. State 14 and Filter Estimate for Study 1 | H-3 |
| H.5. State 14 Filter Estimation Error and Filter Uncertainty for Study 1 . . . | H-3 |
| H.6. State 14 Monte Carlo Study of Filter Error for Study 1 | H-3 |
| H.7. RMS Phase Distortion Before and After Correction, Study 1 | H-4 |
| H.8. Monte Carlo Study of RMS Phase Distortion Before and After Correction, Study 1 | H-4 |
| H.9. Monte Carlo Study of RMS Phase Distortion Caused by Filter Error, Study 1 | H-4 |
| H.10. State 1 and Filter Estimate for Study 2 | H-5 |
| H.11. State 1 Filter Estimation Error and Filter Uncertainty for Study 2 . . . | H-5 |
| H.12. State 1 Monte Carlo Study of Filter Error for Study 2 | H-5 |
| H.13. State 14 and Filter Estimate for Study 2 | H-6 |
| H.14. State 14 Filter Estimation Error and Filter Uncertainty for Study 2 . . . | H-6 |
| H.15. State 14 Monte Carlo Study of Filter Error for Study 2 | H-6 |
| H.16. RMS Phase Distortion Before and After Correction, Study 2 | H-7 |

| Figure | Page |
|---|------|
| H.17. Monte Carlo Study of RMS Phase Distortion Before and After Correction, Study 2 | H-7 |
| H.18. Monte Carlo Study of RMS Phase Distortion Caused by Filter Error, Study 2 | H-7 |
| H.19. State 1 and Filter Estimate for Study 3 | H-8 |
| H.20. State 1 Filter Estimation Error and Filter Uncertainty for Study 3 . . | H-8 |
| H.21. State 1 Monte Carlo Study of Filter Error for Study 3 | H-8 |
| H.22. State 14 and Filter Estimate for Study 3 | H-9 |
| H.23. State 14 Filter Estimation Error and Filter Uncertainty for Study 3 . . | H-9 |
| H.24. State 14 Monte Carlo Study of Filter Error for Study 3 | H-9 |
| H.25. RMS Phase Distortion Before and After Correction, Study 3 | H-10 |
| H.26. Monte Carlo Study of RMS Phase Distortion Before and After Correction, Study 3 | H-10 |
| H.27. Monte Carlo Study of RMS Phase Distortion Caused by Filter Error, Study 3 | H-10 |
| H.28. State 1 and Filter Estimate for Study 4 | H-11 |
| H.29. State 1 Filter Estimation Error and Filter Uncertainty for Study 4 . . | H-11 |
| H.30. State 1 Monte Carlo Study of Filter Error for Study 4 | H-11 |
| H.31. State 14 and Filter Estimate for Study 4 | H-12 |
| H.32. State 14 Filter Estimation Error and Filter Uncertainty for Study 4 . . | H-12 |
| H.33. State 14 Monte Carlo Study of Filter Error for Study 4 | H-12 |
| H.34. RMS Phase Distortion Before and After Correction, Study 4 | H-13 |
| H.35. Monte Carlo Study of RMS Phase Distortion Before and After Correction, Study 4 | H-13 |
| H.36. Monte Carlo Study of RMS Phase Distortion Caused by Filter Error, Study 4 | H-13 |
| H.37. State 1 and Filter Estimate for Study 5 | H-14 |
| H.38. State 1 Filter Estimation Error and Filter Uncertainty for Study 5 . . | H-14 |
| H.39. State 1 Monte Carlo Study of Filter Error for Study 5 | H-14 |

| Figure | Page |
|---|-------|
| H.40. State 14 and Filter Estimate for Study 5 | II-15 |
| H.41. State 14 Filter Estimation Error and Filter Uncertainty for Study 5 . . | II-15 |
| H.42. State 14 Monte Carlo Study of Filter Error for Study 5 | II-15 |
| H.43. RMS Phase Distortion Before and After Correction, Study 5 | II-16 |
| H.44. Monte Carlo Study of RMS Phase Distortion Before and After Correction, Study 5 | II-16 |
| H.45. Monte Carlo Study of RMS Phase Distortion Caused by Filter Error, Study 5 | II-16 |
| H.46. State 1 and Filter Estimate for Study 6 | II-17 |
| H.47. State 1 Filter Estimation Error and Filter Uncertainty for Study 6 . . | II-17 |
| H.48. State 1 Monte Carlo Study of Filter Error for Study 6 | II-17 |
| H.49. State 14 and Filter Estimate for Study 6 | II-18 |
| H.50. State 14 Filter Estimation Error and Filter Uncertainty for Study 6 . . | II-18 |
| H.51. State 14 Monte Carlo Study of Filter Error for Study 6 | II-18 |
| H.52. RMS Phase Distortion Before and After Correction, Study 6 | II-19 |
| H.53. Monte Carlo Study of RMS Phase Distortion Before and After Correction, Study 6 | II-19 |
| H.54. Monte Carlo Study of RMS Phase Distortion Caused by Filter Error, Study 6 | II-19 |
| H.55. State 1 and Filter Estimate for Study 7 | II-20 |
| H.56. State 1 Filter Estimation Error and Filter Uncertainty for Study 7 . . | II-20 |
| H.57. State 1 Monte Carlo Study of Filter Error for Study 7 | II-20 |
| H.58. State 14 and Filter Estimate for Study 7 | II-21 |
| H.59. State 14 Filter Estimation Error and Filter Uncertainty for Study 7 . . | II-21 |
| H.60. State 14 Monte Carlo Study of Filter Error for Study 7 | II-21 |
| H.61. RMS Phase Distortion Before and After Correction, Study 7 | II-22 |
| H.62. Monte Carlo Study of RMS Phase Distortion Before and After Correction, Study 7 | II-22 |

| Figure | Page |
|---|-------|
| H.63. Monte Carlo Study of RMS Phase Distortion Caused by Filter Error, Study 7 | II-22 |
| H.64. State 1 and Filter Estimate for Study 8 | II-23 |
| H.65. State 1 Filter Estimation Error and Filter Uncertainty for Study 8 . . | H-23 |
| H.66. State 1 Monte Carlo Study of Filter Error for Study 8 | H-23 |
| H.67. State 14 and Filter Estimate for Study 8 | II-24 |
| H.68. State 14 Filter Estimation Error and Filter Uncertainty for Study 8 . . | II-24 |
| H.69. State 14 Monte Carlo Study of Filter Error for Study 8 | II-24 |
| H.70. RMS Phase Distortion Before and After Correction, Study 8 | H-25 |
| H.71. Monte Carlo Study of RMS Phase Distortion Before and After Correction, Study 8 | H-25 |
| H.72. Monte Carlo Study of RMS Phase Distortion Caused by Filter Error, Study 8 | II-25 |
| H.73. State 1 and Filter Estimate for Study 9 | H-26 |
| H.74. State 1 Filter Estimation Error and Filter Uncertainty for Study 9 . . | H-26 |
| H.75. State 1 Monte Carlo Study of Filter Error for Study 9 | H-26 |
| H.76. State 14 and Filter Estimate for Study 9 | H-27 |
| H.77. State 14 Filter Estimation Error and Filter Uncertainty for Study 9 . . | H-27 |
| H.78. State 14 Monte Carlo Study of Filter Error for Study 9 | H-27 |
| H.79. RMS Phase Distortion Before and After Correction, Study 9 | H-28 |
| H.80. Monte Carlo Study of RMS Phase Distortion Before and After Correction, Study 9 | H-28 |
| H.81. Monte Carlo Study of RMS Phase Distortion Caused by Filter Error, Study 9 | H-28 |

List of Tables

| Table | Page |
|--|------|
| 2.1. Calculated Coherence Length | 2-7 |
| 2.2. Zernike Functions | 2-11 |
| 2.3. Zernike Function Names | 2-12 |
| 2.4. Dimensionalities of State-Space Matrices and Vectors | 2-17 |
| 3.1. AFWL Deformable Mirror Characteristics | 3-6 |
| 3.2. Measurement Noise Strengths | 3-26 |
| 4.1. Continuous State-Space Model | 4-2 |
| 4.2. Dimensionality of Kalman Filter Vectors and Matrices | 4-3 |
| 4.3. Filter State Transition Matrix and Discrete Driving Noise | 4-5 |
| 5.1. Truth and Filter Model Measurement Noise Strengths | 5-2 |
| 5.2. Summary of Adaptive Optics System Simulated Performance | 5-11 |
| B.1. Percent of Phase Distortion Modeled | B-4 |
| D.1. Atmospheric Distortion State-Space Model | D-7 |

List of Symbols

| Symbol | Page |
|---|------|
| λ | 1-3 |
| $\mathcal{E}[\cdot]$ | 2-3 |
| τ | 2-3 |
| $\mathcal{D}(\tau)$ | 2-3 |
| $\underline{\mathbf{r}}$ | 2-3 |
| $\underline{\rho}$ | 2-3 |
| $\mathcal{D}(\underline{\rho})$ | 2-3 |
| C_n^2 | 2-4 |
| r_0 | 2-6 |
| ζ | 2-6 |
| k | 2-7 |
| ϕ | 2-9 |
| r | 2-9 |
| Θ | 2-9 |
| x | 2-9 |
| y | 2-9 |
| $Z_i(r, \Theta)$ | 2-10 |
| $a_i(t)$ | 2-10 |
| δ_{ij} | 2-12 |
| $\underline{\mathbf{a}}$ | 2-13 |
| $\dot{\underline{\mathbf{x}}}(t)$ | 2-16 |
| $\underline{\mathbf{x}}(t)$ | 2-16 |
| $\mathbf{F}(t)$ | 2-16 |
| $\underline{\mathbf{u}}(t)$ | 2-16 |
| $\mathbf{B}(t)$ | 2-16 |

| Symbol | Page |
|----------------------------------|------|
| $\underline{w}(t)$ | 2-16 |
| $G(t)$ | 2-16 |
| $\underline{z}(t_i)$ | 2-16 |
| $H(t_i)$ | 2-16 |
| $\underline{v}(t_i)$ | 2-16 |
| $Q(t)$ | 2-16 |
| $\delta()$ | 2-16 |
| $R(t_i)$ | 2-16 |
| $\Phi(t_{i+1} - t_i)$ | 2-18 |
| $\underline{w}_d(t_i)$ | 2-18 |
| Q_d | 2-18 |
| B_d | 2-18 |
| $X(t_i)$ | 2-19 |
| $U(t_i)$ | 2-19 |
| X_f | 2-19 |
| P | 2-20 |
| $K(t_i)$ | 2-20 |
| \underline{z}_i | 2-20 |
| $G_c^*(t_i)$ | 2-21 |
| K_c | 2-21 |
| $\underline{x}_a(t)$ | 3-2 |
| $\underline{a}_a(t)$ | 3-3 |
| A | 3-3 |
| X_A, Y_A | 3-9 |
| $u_{-1}(\cdot)$ | 3-9 |
| f | 3-9 |
| M | 3-12 |

| Symbol | Page |
|-----------------------------------|------|
| s | 3-15 |
| $\phi_m(X, Y, t)$ | 3-17 |
| $\text{diag}[\cdot]$ | 3-19 |
| \mathbf{I} | 3-20 |
| \mathbf{H}' | 3-20 |
| L | 3-23 |
| \mathbf{N} | 3-25 |
| k | D-2 |
| L | D-2 |
| R | D-2 |
| N | D-2 |
| $\Phi_n(K)$ | D-2 |
| $W(\rho; 2)$ | D-2 |
| $G_p(\underline{\rho})$ | D-2 |
| $J_o(\cdot)$ | D-2 |
| \underline{y} | D-2 |

Abstract

This thesis considers the design of a linear quadratic Gaussian (LQG) controller for a ground-based adaptive-optics telescope. The incoming aberrated image is reflected from a 97-actuator deformable piezoelectric mirror, then measured with a Hartmann-type wavefront sensor. A Kalman filter processes the outputs of the wavefront sensor and obtains estimates of system states. A linear-quadratic (LQ) regulator processes these state estimates and determines an appropriate set of commands for the deformable mirror.

Atmospheric distortion is modeled as a set of fourteen Zernike coefficients whose dynamic behavior is produced by excitation of a set of shaping filters by zero-mean Gaussian white noise. The response of the mirror to control voltages is modeled as a set of Zernike coefficients whose dynamics are modeled as deterministic first-order systems. The entire control system is simulated using the Multimode Simulation for Optimal Filter Evaluation (MSOFE) software.

DESIGN OF A LINEAR QUADRATIC GAUSSIAN CONTROL LAW FOR AN ADAPTIVE OPTICS SYSTEM

I. Introduction

1.1 Motivation

Certain aspects of the Air Force mission require high-resolution imaging of distant objects. The resolution attainable is theoretically diffraction limited by the receiving aperture. From physics, this diffraction limited resolution is a function of both the diameter of the aperture and the wavelength of light. The larger the ratio of aperture diameter to wavelength, the better the resolution. When some or all of the space between the object and aperture contains turbulent atmosphere, as with ground-based imaging of celestial bodies, the resolution is degraded considerably—the image wanders, becomes fuzzy and distorted, and undergoes intensity fluctuations [2]. It has been reported [13:360] that, on the average, these effects may degrade resolution of larger telescopes to two arc seconds or more, corresponding to diffraction-limited viewing through only a 6-cm aperture. One obvious approach to overcoming atmospheric distortion is to place the telescope above the atmosphere. An example of this approach is the Hubble space telescope.

The Air Force Weapons Laboratory (AFWL) at Kirtland AFB, NM, the Rome Air Development Center (RADC) at Griffis AFB, NY, and a number of other Government and private institutions are interested in compensating for these deleterious effects by using adaptive optics in the receiving optical system. Adaptive optics is the use of active optical components for compensation of unwanted time-varying optical characteristics. For example, an automatic focus mechanism in a 35-mm camera is an adaptive optics system. In particular, the AFWL is actively pursuing the use of adaptive optics using deformable mirrors for ground-based observation of orbiting satellites, and is the sponsor of this research.

1.2 Research Objective

The overall objective of this research is to develop a Linear Quadratic Gaussian (LQG) control law for an adaptive optics system. Such a control law provides optimal control in the sense of minimizing a defined cost function associated with deviation from desired behavior. LQG also accounts for uncertainty in measurements and the stochastic nature of the state dynamics. A detailed discussion of LQG control is available in the literature [25]. To achieve the LQG design, several tasks are required:

1. Define a state space on which to base design and analysis.
2. Develop the stochastic equations which model the open-loop system.
3. Develop the LQG control law.
4. Simulate and evaluate the controlled, closed-loop system.

The first task involves determining a method of quantifying distortion of a time-varying image. The method should account for most of the distortion using as few states as possible. The states should also be conducive to measurement. Once the states are identified, the second task is to represent the stochastic nature of their dynamics and measurements in a set of equations (models) which describe the random nature of the processes. Key components of such a model are atmospheric distortion, mirror response, and wavefront sensing. Wherever practical, the research uses actual data from the deformable mirror apparatus currently in the optics development laboratory at the AFWL. Once these open-loop "truth" models are developed, the actual controller can be designed. This task includes definition of an appropriate cost function, design of a Kalman filter—possibly of reduced order—to estimate system states and covariances, and design of a linear-quadratic (LQ) regulator. The final task includes simulation of the complete system. This will involve implementing the truth models, Kalman filter, and controller in software capable of simulating random processes. Multimode Simulation for Optimal Filter Evaluation (MSOFE) [28] is such a package.

1.3 Assumptions

This research is a proof-of-concept. Several assumptions are necessary in order to carry it out in the allotted time. Some of the assumptions are made based on literature precedent. Many of the assumptions are made to account for lack of data. Other assumptions are engineering judgement.

The first assumption is that the telescope is ground based, and that the application is satellite-viewing. A second assumption is that a separate control system is responsible for keeping the telescope pointed at the satellite. It is assumed the telescope is using a visible point source of light at or near the satellite as a reference, and that anisoplanatism is negligible, i.e., the light from the reference traverses the same atmosphere as the light from the satellite. This implies that deforming the mirror to improve the reference image will also sharpen the satellite image. The wavelength λ of the reference image light is assumed to be 514 nanometers (nm), the value used during laboratory evaluation of the hardware [22].

The deformable mirror is a 97-element piezoelectric mirror whose actuators are arranged in evenly-spaced rows and columns. Furthermore, based on limited data, it is assumed the actuators are linear, and that all actuator influence functions are identical and symmetric. The effects of additional factors (lenses, vibrations, etc.) are not modeled. In an actual telescope, separate active tilt mirrors may precede the deformable mirror. These non-deformable tilt mirrors remove the gross tilts of the overall image. This research does not explicitly model these mirrors, but assumes they remove 95 % of the gross tilts.

Although the statistics of atmospheric distortion of images are time varying—for example, there is generally less distortion at night than day—the stochastic model for the atmosphere is assumed time-invariant. This assumption is valid if the duration of the observation is short relative to the time-varying nature of the atmospheric statistics.

Finally, the very nonrestrictive assumption is made that the time delay due to light propagation through the optical components is negligible. The time delay due to finite

sampling time, however, is not negligible. The effect of time delay in the sampling process will not be specifically modeled, but will be used as an upper limit on the sampling rate.

1.4 Treatment

This thesis presents material in a topical fashion. First, Chapter 2 begins by laying the groundwork fundamental to the understanding of atmospheric turbulence and its effect on optical viewing. A qualitative discussion of an adaptive optics system is presented. The remaining portion of Chapter 2 defines the state space used for design and analysis of the control system. Chapter 3 develops stochastic models of the atmospheric distortion, deformable mirror, and wavefront sensor. Chapter 4 presents the design of the LQG control law, and Chapter 5 discusses the closed-loop simulation and evaluation thereof. Chapter 6 presents conclusions of this research and recommendations for future efforts.

II. Background

2.1 Atmospheric Optics

2.1.1 Introduction The atmosphere can have several effects on light traversing it. Certain chemical constituents of the atmosphere may selectively absorb certain frequencies of light and retransmit the energy at different frequencies. If the light is a high-energy beam such as a high-energy laser, it is possible for the light energy absorbed by the atmosphere to affect the index of refraction in the immediate vicinity of the beam, which in turn affects the shape of the beam profile. This phenomenon is known as blooming [41:223]. In the presence of aerosols, light may experience spatial discontinuities in the direction of propagation, a phenomenon known as scattering. Finally, in imaging applications, the turbulence of the atmosphere can cause continuous spatial and temporal variations in the index of refraction along the ray path, resulting in temporal and spatial modulation of the received intensity and phase. The modulation of intensity is known as scintillation [5:37], an example of which is the twinkling of stars [37:224] [36:3]. As a rule of thumb, scintillation effects can be considered insignificant when the wavelength λ , propagation distance through turbulence L , and telescope entrance aperture diameter D , are related by [44:2580] [45:819] :

$$\sqrt{\lambda L} \ll D \quad (2.1)$$

For example, for an atmospheric propagation distance of 20,500 meters [38:A4], wavelength of 514 nanometers and a telescope diameter of 1 meter, the result is a less severe inequality $0.102 < 1.0$. Nevertheless, much of the literature [9:1435] [29] [47:3] [16] suggests the intensity modulation is negligible. The modulation of phase is the leading contributor to image wandering, fuzziness, and distortion. This research is therefore limited to correction of phase.

2.1.2 Turbulence The physical property of an air parcel which most influences phase of propagating light is its index of refraction. This, in turn, is a function of various physical parameters such as temperature, pressure, humidity, and wavelength, to name a few. Empirical equations describing the dependence of the index of refraction on these

parameters are generally available [5:10] [18:531] [31:101]. In the turbulent atmosphere these physical parameters are generally functions of time and space, and hence index of refraction is also a function of time and space. Because of the random nature of turbulence, there is no deterministic expression of this relationship.

A popular representation [5:12] [18:336] of atmospheric turbulence considers the atmosphere to consist of many parcels or "eddies" of air moving with respect to each other. The sizes of these eddies change with time; the larger ones generally dissipate into smaller ones. Eventually, the eddies become small enough such that their kinetic energy dissipates into heat. The sizes of the eddies are characterized relative to L_0 and l_0 , quantities having units of length and known as the "outer scale" and "inner scale" of turbulence, respectively. Eddies larger than the outer scale are anisotropic and are formed by wind shear and temperature gradients. An anisotropic eddy has spatial statistics which depend on direction [18:338]. These eddies are said to lie in the "input range" since they represent newly-formed eddies, inputs to atmospheric turbulence. For eddies smaller than L_0 but larger than l_0 , kinetic energy effects are more significant than viscosity effects, and the turbulence is essentially isotropic. An isotropic eddy has spatial statistics which do not depend on direction. Eddies of this size are said to be in the "inertial subrange" since inertia is significant relative to friction. When the size of the eddy is less than l_0 , viscosity effects dominate over kinetic effects, and the eddy is said to be in the "dissipation range" [18:336]. At low altitude L_0 is on the order of meters, whereas l_0 is on the order of millimeters. Both the local inner and outer scales of turbulence generally increase with altitude [5:12]. Light propagating vertically through the atmosphere, therefore, encounters eddies of various sizes and of various subranges. The end result is a randomly-distorted image whose degree of distortion is not known without measurement.

2.1.3 Structure Functions The statistics of atmospheric turbulence are often represented as "structure functions" [37]. The presentation of the structure function here closely follows that of Tatarski [37] and Ishimaru [18]. Any direct quotes are from the latter source.

Some physical characteristics associated with a given location in the turbulent atmosphere can be described as random processes. For example, let $h(t)$ be a random process describing the absolute humidity at a specified location. This random function "... is not strictly stationary." The statistics of $h(t)$ can and generally do change with time. The difference $h(t + \tau) - h(t)$, however, is considered stationary. This property is accurate for many atmospheric variables. Thus it can be said the function $h(t)$ has stationary increments:

$$\mathcal{E} [h(t + \tau) - h(t)] = f(\tau) \quad (2.2)$$

where $\mathcal{E} [\cdot]$ represents the expectation operator and $f(\tau)$ is a function of the time difference, τ . The *temporal structure function* for this example, $\mathcal{D}(\tau)$, is defined as:

$$\mathcal{D}_h(\tau) = \mathcal{E} [|h(t + \tau) - h(t)|^2] \quad (2.3)$$

The correlation function is a more familiar statistical relation:

$$\mathcal{B}_h(t_1, t_2) = \mathcal{E} [h(t_1)h(t_2)] \quad (2.4)$$

and is related to the structure function by:

$$\mathcal{D}_h(\tau) = \mathcal{B}_h(t + \tau, t + \tau) + \mathcal{B}_h(t, t) - \mathcal{B}_h(t + \tau, t) - \mathcal{B}_h(t, t + \tau) \quad (2.5)$$

The spatial analog to the random process with stationary increments is the "locally homogeneous" random function. For example, let $h(\underline{\mathbf{r}})$ be a random "process" describing the absolute humidity at a specified time at location $\underline{\mathbf{r}}$. For convenience the $h(\cdot)$ function symbology is reused here. This random function "... is not strictly homogeneous." The statistics of $h(\underline{\mathbf{r}})$ can and generally do change with location. The difference $h(\underline{\mathbf{r}} + \underline{\rho}) - h(\underline{\mathbf{r}})$, however, is homogeneous. Thus the function $h(\underline{\mathbf{r}})$ is said to be locally homogeneous. The *spatial structure function* for this example, $\mathcal{D}(\underline{\rho})$, is:

$$\mathcal{D}_h(\underline{\rho}) = \mathcal{E} [|h(\underline{\mathbf{r}} + \underline{\rho}) - h(\underline{\mathbf{r}})|^2] \quad (2.6)$$

where the $\mathcal{D}_h(\cdot)$ symbology is reused for convenience. If the process is isotropic as well as locally homogeneous, the spatial structure function depends only on the magnitude of the spatial separation:

$$\mathcal{D}_h(\rho) = \mathcal{E} \left[\left| h(\underline{\mathbf{r}} + \underline{\rho}) - h(\underline{\mathbf{r}}) \right|^2 \right], \quad \rho = \|\underline{\rho}\| \quad (2.7)$$

A key assumption in applying the temporal and spatial structure functions to atmospheric turbulence is the concept of “frozen turbulence” [5:17], also known as “Taylor’s hypothesis” [19:133]. This assumption implies the temporal fluctuations in various meteorological variables at a given location are caused by a “snapshot” realization of spatial fluctuations flowing by. Taylor’s hypothesis is “usually a good approximation for optical propagation through the atmosphere.” [19:133]

2.1.4 Kolmogorov Statistics The index of refraction n at a location $\underline{\mathbf{r}}$ can be expressed as the sum of the mean and a fluctuation about the mean [5:17]:

$$n(\underline{\mathbf{r}}) = \mathcal{E} [n(\underline{\mathbf{r}})] + n_1(\underline{\mathbf{r}}) \quad (2.8)$$

where $n_1(\underline{\mathbf{r}})$ is a zero-mean Gaussian random variable. The spatial structure function for the isotropic random variable describing the index of refraction fluctuation is:

$$\mathcal{D}_{n_1}(\rho) = \mathcal{E} \left[\left| n_1(\underline{\mathbf{r}} + \underline{\rho}) - n_1(\underline{\mathbf{r}}) \right|^2 \right] \quad (2.9)$$

The unity subscript in Equation (2.9) is often omitted, with the fluctuation definition implied.

Kolmogorov’s famous result, as described by several references [6:155] [2:11] [17:22] [31:101] [34:288] [5:19] [19:526] [9:1430], is that, for spatial separation within the inertial subrange $l_0 \ll \rho \ll L_0$, Equation (2.9) is closely approximated by:

$$\mathcal{D}_n(\rho) = C_n^2 \rho^{2/3} \quad (2.10)$$

where C_n^2 is the refractive index structure constant, a parameter which indicates the degree to which atmospheric turbulence affects optical propagation [34:288]. C_n^2 is generally modeled as a function of altitude and time of day [5:20]; several models describe it as functions

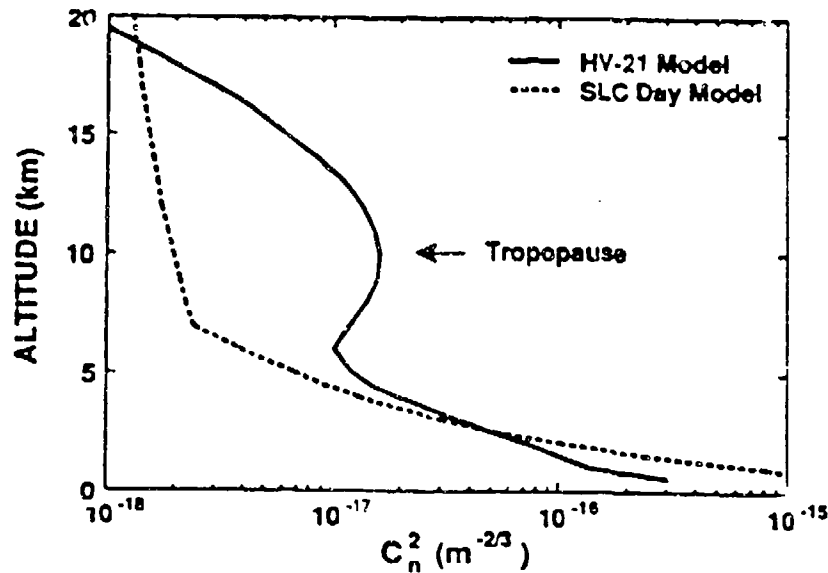


Figure 2.1. Refractive Index Structure Constant

thereof [33:290] [5:20] [6] [37:A4] [30:102]. Two such models are the SLC-Day model and the Hufnagel-Stanley model [30:102]. Figure 2.1 shows that these widely-accepted models are in less than perfect agreement, and that the altitude dependency of C_n^2 varies over three orders of magnitude [30].

Since the phase of a wavefront is of interest for many adaptive optics applications, one may wonder if it has a structure function. Fried [9:1430] discusses the phase structure function:

$$D_\phi(\rho) = \mathcal{E} \left[\left| \phi(\underline{r} + \underline{\rho}) - \phi(\underline{r}) \right|^2 \right] \quad (2.11)$$

which is actually defined as a phase *fluctuation* structure function, since ϕ is the deviation of phase about the aperture-averaged phase. Based on the Kolmogorov turbulence model and neglecting intensity fluctuations, Fried writes:

$$D_\phi(\rho) = A\rho^{5/3} \quad (2.12)$$

where the parameter \mathcal{A} depends on propagation path, wavelength, and environmental conditions. He then defines the coherence length parameter r_0 in terms of \mathcal{A} :

$$r_0 = (6.88/\mathcal{A})^{3/5} \quad (2.13)$$

and thus:

$$\mathcal{D}_\phi(\rho) = 6.88(\rho/r_0)^{5/3} \quad (2.14)$$

This r_0 parameter is generally known as Fried's coherence length in the later literature [29:209] [11:550] [40:1774] [17:1596] [31:102]. He describes it as the "diameter of a heterodyne collector for which distortion effects begin to seriously limit performance". Another interpretation is that it is the diameter of an aperture such that the rms phase distortion is 1 radian [23]. He finishes his introduction by stating that, for visible and near-IR propagation from an approximately zenith source, typical values of r_0 are on the order of a few centimeters.

An equation for the coherence length in terms of other parameters is given by Parenti [31:102]:

$$r_0 = 0.185 \left(\frac{\lambda^2}{\sec(\zeta) \int dh C_n^2(h)} \right)^{3/5} \quad (2.15)$$

where

| | | |
|------------|---|---|
| r_0 | = | Fried's coherence length (m) |
| λ | = | wavelength (m) |
| ζ | = | zenith angle of source (rad) |
| $C_n^2(h)$ | = | refractive index structure constant ($\text{m}^{-2/3}$) |
| h | = | altitude (m) |

Wang and Markey [46:78] give a simplified equation for r_0 where propagation is from the zenith and the refractive index structure constant is assumed to be constant along the path:

$$r_0 = 1.68(C_n^2 z k^2)^{-3/5} \quad (2.16)$$

where

| | | |
|---------|---|---|
| z | = | path length through turbulence (m) |
| k | = | wavenumber = $2\pi/\lambda$ (m^{-1}) |
| ζ | = | zenith angle of source (rad) |

Walters and others [42:828] present some measured values of r_0 for vertical paths at mountaintop sites in the White Sands, New Mexico region. The nighttime average (over a seven-month period) was found to be $9.0 \text{ cm} \pm 4.0 \text{ cm}$ ($1\text{-}\sigma$); the daytime average was $4.5 \text{ cm} \pm 1.8 \text{ cm}$ ($1\text{-}\sigma$). Starlight was used as the light source.

Parenti [31:104] gives some estimates of r_0 derived from the Hufnagel-Valley and SLC-Day models of $C_n^2(h)$ at 500-nm wavelength and two zenith angles. These are shown in Table 2.1.

Table 2.1. Calculated Coherence Length

| Model | Zenith Angle | r_0 |
|---------|--------------|--------|
| HV-21 | 0° | 5.0 cm |
| HV-21 | 45° | 4.0 cm |
| SLC-Day | 0° | 5.1 cm |
| SLC-Day | 45° | 4.1 cm |

The significance of the development presented thus far is that the effect of atmospheric turbulence on optical viewing is complex. The time behavior of the quality of the received image depends on many factors such as the wavelength, altitude-dependent structure function constant, zenith angle, and altitude of the telescope. The wind velocity and its altitude distribution also affect image quality. In addition, satellite motion with respect to the observer is a factor. The introductory discussion presented thus far could continue to the point of having an analytically-derived statistical model of the effect of atmospheric turbulence on image quality, but the mathematical rigor is beyond the scope of this research. The reader is referred to the literature for an appreciation of the rigor involved [16]. The significant result is that no single model will be accurate for all possible atmospheric conditions. The use of multiple models will be briefly discussed in Chapter VI.

2.2 *Zernike Functions*

2.2.1 *Introduction* It is obviously necessary to have some means of expressing the phase distortion present in an image. This section develops the use of the Zernike basis functions as such a means.

Assume a circular aperture of diameter D is pointed at a coherent, monochromatic point source of light located a distance L away. Further assume that L is much greater than D . If there are no distortive elements along the propagation path, the phase of the incident wave within the aperture would be spatially constant, i.e., the phase of any two points within the aperture would be the same. It could also be said for such a case, that the phase at any point within the aperture is equal to the spatially averaged phase. Figure 2.2 shows a two-dimensional representation of this situation.

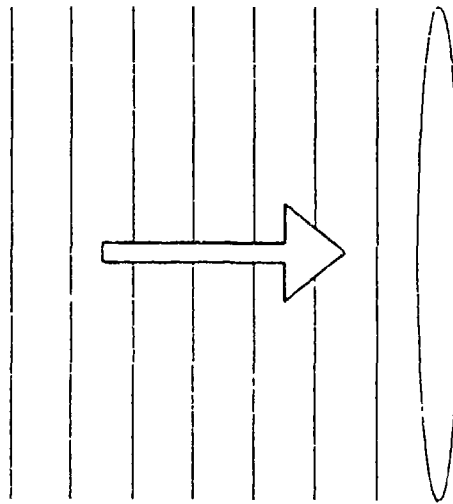


Figure 2.2. Planar Wavefronts at an Aperture

If a turbulent atmosphere is now introduced into some or all of the space between source and observer, the wavefronts at the aperture will be distorted, i.e., two points within the aperture will not necessarily have the same phase. Furthermore the phase at any point within the aperture will not necessarily equal the spatially averaged phase. Figure 2.3 shows a two-dimensional representation of this situation.

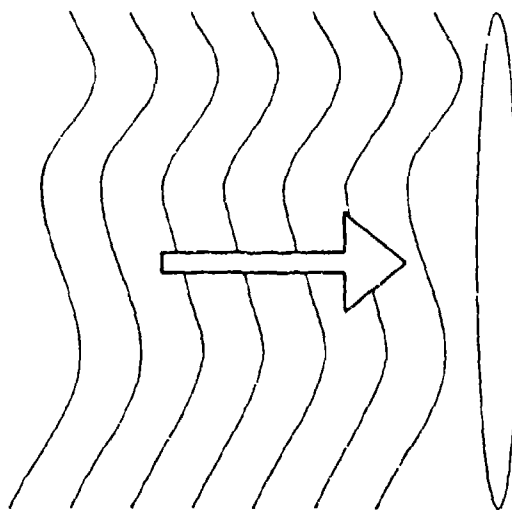


Figure 2.3. Distorted Wavefronts at an Aperture

The absolute phase of the electromagnetic wave in the aperture is a function of time and of the spatial (polar or rectangular) coordinates within the aperture:

$$\phi \Rightarrow \phi(r, \Theta, t) \quad (2.17)$$

$$\phi \Rightarrow \phi(x, y, t) \quad (2.18)$$

where

| | | | |
|----------|---|--------------------|----------------------|
| ϕ | = | absolute phase | |
| r | = | radial distance | = $\sqrt{x^2 + y^2}$ |
| Θ | = | angular coordinate | = $\tan^{-1}(y/x)$ |
| x | = | x-coordinate | = $r \cos(\Theta)$ |
| y | = | y-coordinate | = $r \sin(\Theta)$ |

The functions represented by Equations (2.17) and (2.18) do not have identical functional forms; both functions are given the same name ϕ for convenience. Phase can be expressed in units of degrees, radians, or wavelengths. Likewise, x , y , and r can be expressed in units of wavelengths or the length normalized by the radius of the aperture.

The right-hand sides of Equations (2.17) and (2.18) are expressible in several ways. One option might be to sample the phase at numerous locations in the plane and let the vector of samples define the shape of the phase function. This "vector space" approach has been used by AFIT researchers [3] [12] [27] [33]. Another approach, the one taken in this research, is to express the phase as a sum of functions:

$$\phi(r, \Theta, t) = \sum_{i=0}^N F_i(r, \Theta, t) \quad (2.19)$$

More conveniently, the phase can be expressed as a linear combination of basis functions:

$$\phi(r, \Theta, t) = \sum_{i=0}^N a_i(t) Z_i(r, \Theta) \quad (2.20)$$

where the $Z_i(r, \Theta)$ are basis functions which span the functional space containing $\phi(r, \Theta)$, and the $a_i(t)$ are the coefficients. The choice of which set of basis functions to use is a design decision. Some mentioned in the literature include Legendre [35], Karhunen-Loeve [29] [43] [46], and Zernike [4] [9] [16] [46] [44] [7] [45] [15] [38] functions. In the case of turbulence modeled with Kolmogorov statistics, the Karhunen-Loeve functions are not analytic [29:210]. The Zernike set of basis functions, analytic by definition, are used as basis functions in this research.

2.2.2 Zernike Functions The Zernike functions are the $Z_i(r, \Theta)$ of Equation (2.20). Each Zernike function is a real-valued, dimensionless, deterministic function of position within the aperture. The $a_i(t)$ are the Zernike *coefficients*. Each Zernike coefficient is a real-valued function of time, with units of wavelength for this research. The i -th Zernike function can be expressed as the product of a radial function and an azimuthal function [4]:

$$Z_i(r, \Theta) = f_i(r) g_i(\Theta) \quad (2.21)$$

Details of generating the radial and azimuthal functions of Equation (2.21) are available in the literature [38:79][4]. Table 2.2 presents the first fifteen Zernike functions (0—14) along with their radial and azimuthal order, n and m , respectively. The functions are also expressed in rectangular coordinates as well. Three-dimensional plots of the first fifteen

Table 2.2. Zernike Functions

| i | n | m | $Z_i(r, \Theta)$ | $Z_i(x, y)$ |
|----|---|---|--|--|
| 0 | 0 | 0 | 1 | 1 |
| 1 | 1 | 1 | $2(\frac{r}{R}) \cos(\Theta)$ | $\frac{2}{R}x$ |
| 2 | 1 | 1 | $2(\frac{r}{R}) \sin(\Theta)$ | $\frac{2}{R}y$ |
| 3 | 2 | 0 | $\sqrt{3}(2(\frac{r}{R})^2 - 1)$ | $\frac{\sqrt{3}}{R^2}(2x^2 + 2y^2 - R^2)$ |
| 4 | 2 | 2 | $\sqrt{6}(\frac{r}{R})^2 \sin(2\Theta)$ | $\frac{2\sqrt{6}}{R^2}(xy)$ |
| 5 | 2 | 2 | $\sqrt{6}(\frac{r}{R})^2 \cos(2\Theta)$ | $\frac{\sqrt{6}}{R^2}(x^2 - y^2)$ |
| 6 | 3 | 1 | $\sqrt{8}(3(\frac{r}{R})^3 - 2(\frac{r}{R})) \sin(\Theta)$ | $\frac{\sqrt{8}}{R^3}(3x^2 + 3y^2 - 2R^2)y$ |
| 7 | 3 | 1 | $\sqrt{8}(3(\frac{r}{R})^3 - 2(\frac{r}{R})) \cos(\Theta)$ | $\frac{\sqrt{8}}{R^3}(3x^2 + 3y^2 - 2R^2)x$ |
| 8 | 3 | 3 | $\sqrt{8}(\frac{r}{R})^3 \sin(3\Theta)$ | $\frac{\sqrt{8}}{R^3}(3x^2 - y^2)y$ |
| 9 | 3 | 3 | $\sqrt{8}(\frac{r}{R})^3 \cos(3\Theta)$ | $\frac{\sqrt{8}}{R^3}(x^2 - 3y^2)x$ |
| 10 | 4 | 0 | $\sqrt{5}(6(\frac{r}{R})^4 - 6(\frac{r}{R})^2 + 1)$ | $\frac{\sqrt{5}}{R^4}(6(x^2 + y^2)^2 - 6R^2(x^2 + y^2) + R^4)$ |
| 11 | 4 | 2 | $\sqrt{10}(4(\frac{r}{R})^4 - 3(\frac{r}{R})^2) \cos(2\Theta)$ | $\frac{\sqrt{10}}{R^4}(4x^2 + 4y^2 - 3R^2)(x^2 - y^2)$ |
| 12 | 4 | 2 | $\sqrt{10}(4(\frac{r}{R})^4 - 3(\frac{r}{R})^2) \sin(2\Theta)$ | $\frac{2\sqrt{10}}{R^4}(4x^2 + 4y^2 - 3R^2)xy$ |
| 13 | 4 | 4 | $\sqrt{10}(\frac{r}{R})^4 \cos(4\Theta)$ | $\frac{\sqrt{10}}{R^4}(x^4 - 6x^2y^2 + y^4)$ |
| 14 | 4 | 4 | $\sqrt{10}(\frac{r}{R})^4 \sin(4\Theta)$ | $\frac{4\sqrt{10}}{R^4}(x^2 - y^2)xy$ |

Zernike function are shown in Appendix A.

One advantage of using the Zernike functional space is that the functions correspond to aberrations commonly studied in optics [20:196]. Table 2.3 shows the names of the more common ones. By convention, x-tilt is defined in this research to be tilt about the x-axis.

The Zernike functions form an orthogonal basis set which satisfies [38:79]:

$$\frac{1}{\pi R^2} \int_0^{2\pi} d\Theta \int_0^R dr r Z_i(r, \Theta) Z_j(r, \Theta) = \delta_{ij} \quad (2.22)$$

Table 2.3. Zernike Function Names

| i | Aberration |
|---|-------------|
| 0 | piston |
| 1 | y-tilt |
| 2 | x-tilt |
| 3 | focus |
| 4 | astigmatism |
| 5 | astigmatism |
| 6 | coma |
| 7 | coma |

where δ_{ij} is the Kronecker delta:

$$\delta_{ij} = \begin{cases} 1, & i = j \\ 0, & i \neq j \end{cases} \quad (2.23)$$

As shown in Appendix C, a consequence of Equation (2.22) is that the root-mean-square (rms) value of phase in an aperture is the square root of the sum of squares of the corresponding Zernike coefficients:

$$\phi_{rms} = \sqrt{a_0^2 + a_1^2 + a_2^2 + \cdots + a_N^2} \quad (2.24)$$

The expansion coefficients for an arbitrary phase associated with Equation (2.20) can be obtained by [38:79]:

$$a_i(t) = \frac{\int d\Theta \int dr r W(r, \Theta) \phi(r, \Theta, t) Z_i(r, \Theta)}{\int d\Theta \int dr r W(r, \Theta)} \quad (2.25)$$

where $W(r, \Theta)$ is the aperture weighting function defined by [38:79]:

$$W(r, \Theta) = \begin{cases} 1 & r \leq R \\ 0 & r > R \end{cases} \quad (2.26)$$

It should be noted that this definition of $W(r, \Theta)$ is selected to be consistent with the scaling coefficients in $Z_i(r, \Theta)$. For a circular aperture of known radius, the phase within the aperture at a given time can also be expressed in shorthand notation as a vector \underline{a} of expansion coefficients:

$$\phi(r, \Theta, t) \Rightarrow \underline{a}^T(t) = \begin{bmatrix} a_0(t) & a_1(t) & a_2(t) & \cdots & a_N(t) \end{bmatrix} \quad (2.27)$$

Post-multiplication of $\underline{a}^T(t)$ by a column vector of $N+1$ Zernike functions is implied in this notation. In general, $N = \infty$ is required to obtain an exact description of an arbitrary phase front in terms of basis functions. Based on spatial Nyquist consideration of the actuator and wavefront sensor geometry for the optics system at the AFWL, and of relative mean square phase error content of each Zernike mode in the presence of Kolmogorov-modeled turbulence (see Appendix B), the truth model in this research is selected to consist of the first fifteen Zernike modes ($N=14$).

As an example of what an arbitrary sum of the first 15 Zernike functions would look like, Figure 2.4 shows a plot of Equation (2.20) for a coefficient vector of:

$$\underline{a}^T(t) = \begin{bmatrix} 20 & 1 & 1 & 1 & 1 & 1 & 1 & 1 & 1 & 1 & 1 & 1 & 1 & 1 & 1 \end{bmatrix} \quad (2.28)$$

The zeroth Zernike mode (i.e. piston) is not a distortive contributor. Also, it is not measurable by the sensor used to measure wavefront distortion. Thus we can subtract the piston contribution from the absolute phase and obtain a functional space which describes the *deviation* in phase from the aperture-average phase. From this point forward, only Zernike modes 1-14 are considered, and $\phi(r, \Theta, t)$ is redefined to be the deviation from aperture-averaged phase, also termed phase *distortion*. Thus, using the shorthand notation introduced earlier:

$$\phi(r, \Theta, t) \Rightarrow \underline{a}^T(t) = \begin{bmatrix} a_1(t) & a_2(t) & \cdots & a_{14}(t) \end{bmatrix} \quad (2.29)$$

Figure 2.5 shows the same plot as Figure 2.4, but with the piston (i.e. average phase) not included.

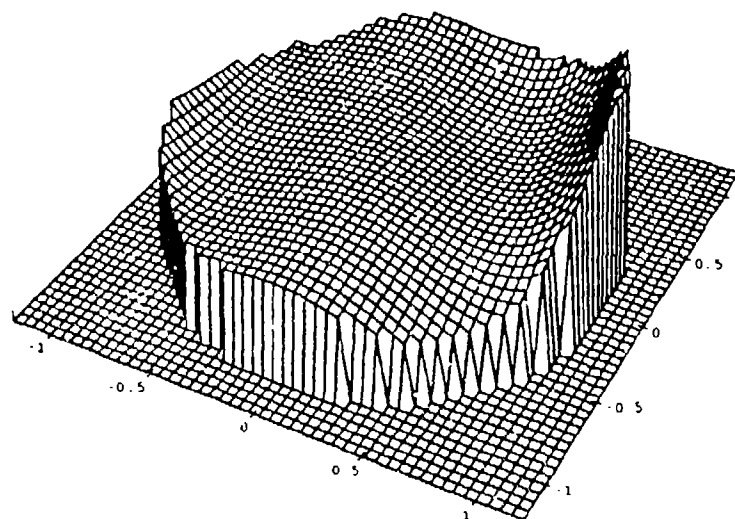


Figure 2.4. Weighted Sum of Zernike Functions 0-14

One final topic is required to be discussed regarding Zernike-function description of optical phase deviation—scaling. The question is, if a large aperture sample of an incoming wavefront is focused into a smaller aperture, what is the effect on the expansion coefficients? The answer is: nothing. For example, consider the geometry of Figure 2.6. Aberrated light from a distant source enters a one-meter radius circular aperture. Assume the aberration consists of ten wavelengths of x-tilt across the aperture. At this large aperture:

$$\phi(x, y) = a_2 Z_2(x, y) = a_2 \frac{2}{R} y = 2 a_2 y \quad (2.30)$$

At $y = 1$ the phase deviation is five wavelengths; therefore $a_2 = 5/2$ for the large aperture.

By passing through a set of perfect lenses, the size of the image is reduced to a circle of 0.1-meter radius. At this small aperture:

$$\phi'(x, y) = a'_2 Z'_2(x, y) = a'_2 \frac{2}{R'} y = 20 a'_2 y \quad (2.31)$$

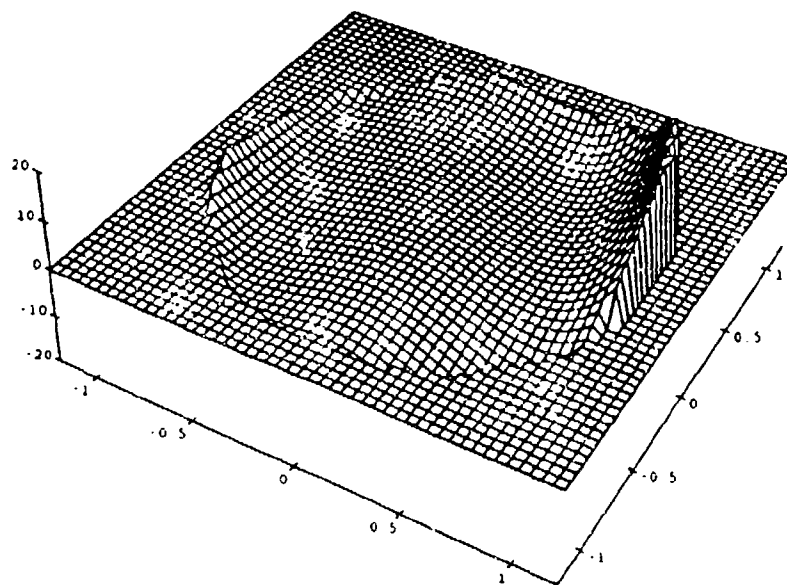


Figure 2.5. Weighted Sum of Zernike Functions 1-14

At $y=0.1$, the phase deviation is still five wavelengths; therefore $a'_2 = 5/2$ for the small aperture as well. This same reasoning can be extended to all the Zernike modes. This aperture invariance is convenient for imaging applications, since generally a large-aperture telescope gathers light, a medium-aperture deformable mirror processes it, and a small-aperture wavefront sensor measures its distortion.

2.3 Stochastic State-Space Modeling

The development of a Linear Quadratic Gaussian (LQG) control law requires a linear stochastic state-space model of the system of interest. The required forms for continuous dynamics and discrete measurements are [24:169]:

$$\dot{\underline{x}}(t) = \underline{F}(t)\underline{x}(t) + \underline{B}(t)\underline{u}(t) + \underline{G}(t)\underline{w}(t) \quad (2.32)$$

$$\underline{z}(t_i) = \underline{H}(t_i)\underline{x}(t_i) + \underline{v}(t_i) \quad (2.33)$$

where

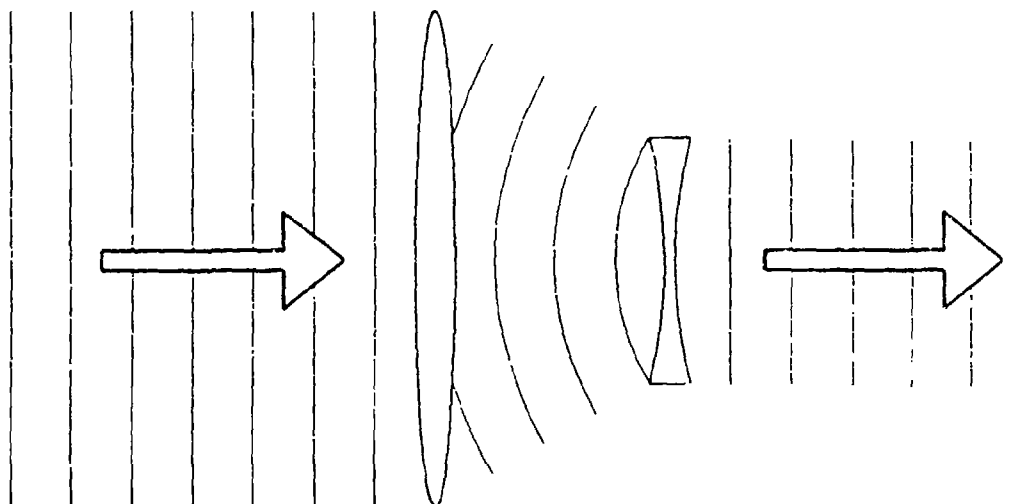


Figure 2.6. Change in Radius

| | | |
|--------------------------|---|---|
| $\dot{\underline{x}}(t)$ | = | time rate-of-change of system state vector |
| $\underline{x}(t)$ | = | system state vector |
| $F(t)$ | = | state dynamics matrix |
| $\underline{u}(t)$ | = | deterministic input vector |
| $B(t)$ | = | input distribution matrix |
| $\underline{w}(t)$ | = | zero-mean white Gaussian driving noise vector |
| $G(t)$ | = | driving noise distribution matrix |
| $\underline{z}(t_i)$ | = | discrete measurement vector |
| $H(t_i)$ | = | discrete output matrix |
| $\underline{v}(t_i)$ | = | zero-mean, discrete-time white Gaussian measurement noise |

The strength of the zero-mean white Gaussian driving noise $\underline{w}(t)$ is defined by [24:155]:

$$\mathcal{E}\{\underline{w}(t)\underline{w}^T(t')\} = \mathbf{Q}(t)\delta(t - t') \quad (2.34)$$

where $\mathbf{Q}(t)$ is the noise strength matrix and $\delta(\)$ is the dirac delta.

The covariance of the zero-mean measurement noise $\underline{v}(t_i)$ is defined by [24:174]:

$$\mathcal{E}\{\underline{v}(t_i)\underline{v}^T(t_j)\} = \mathbf{R}(t_i)\delta_{ij} \quad (2.35)$$

where $\mathbf{R}(t_i)$ is the noise covariance matrix.

The dimensionalities of the vectors and matrices associated with continuous dynamics and discrete measurements are given in Table 2.4 [25:9].

Table 2.4. Dimensionalities of State-Space Matrices and Vectors

| Matrix/Vector | Dimension |
|----------------------|--------------|
| $F(t)$ | $n \times n$ |
| $\underline{x}(t)$ | $n \times 1$ |
| $B(t)$ | $n \times r$ |
| $\underline{u}(t)$ | $r \times 1$ |
| $G(t)$ | $n \times s$ |
| $\underline{w}(t)$ | $s \times 1$ |
| $Q(t)$ | $s \times s$ |
| $\underline{z}(t_i)$ | $m \times 1$ |
| $H(t_i)$ | $m \times n$ |
| $\underline{v}(t_i)$ | $m \times 1$ |
| $R(t_i)$ | $m \times m$ |

If the dynamic system and measurement device are time-invariant, which was assumed for the nominal models of this research, the time-dependence can be dropped from the notation associated with the defining matrices:

$$\dot{\underline{x}}(t) = F\underline{x}(t) + B\underline{u}(t) + G\underline{w}(t) \quad (2.36)$$

$$\underline{z}(t_i) = H\underline{x}(t_i) + \underline{v}(t_i) \quad (2.37)$$

The dynamic driving noise strength and measurement noise variance lose their time-dependency and become Q and R , respectively. Such time invariance implies that the statistical behavior of the system does not change with time.

Kalman filters, which will be discussed shortly, often model the continuous-time system dynamics of Equation (2.36) in the discrete-time domain. An "equivalent" discrete-

time model of the linear system dynamics can be written as [24:171]:

$$\underline{x}(t_{i+1}) = \Phi(t_{i+1} - t_i)\underline{x}(t_i) + \mathbf{B}_d \underline{u}(t_i) + \underline{w}_d(t_i) \quad (2.38)$$

where $\Phi(t_{i+1} - t_i)$ is the $n \times n$, time-invariant state transition matrix associated with \mathbf{F} [24:41] and the zero-mean discretized driving noise $\underline{w}_d(t_i)$ has strength \mathbf{Q}_d defined by [24:171]:

$$\mathcal{E}\{\underline{w}_d(t_i)\underline{w}_d^T(t_j)\} = \mathbf{Q}_d \delta_{ij} = \left[\int_{t_i}^{t_{i+1}} \Phi(t_{i+1} - \tau) \mathbf{G} \mathbf{Q} \mathbf{G}^T \Phi^T(t_{i+1} - \tau) d\tau \right] \delta_{ij} \quad (2.39)$$

The discrete-time input distribution matrix \mathbf{B}_d is defined by [24:171]:

$$\mathbf{B}_d = \int_{t_i}^{t_{i+1}} \Phi(t_{i+1} - \tau) \mathbf{B} d\tau \quad (2.40)$$

Chapter III presents the definitions of these vectors and matrices in terms of the adaptive optics system of this research.

2.4 Linear Quadratic Regulator

The simple LQG regulator concept is based on the assumption that there are costs associated with nonzero states (\underline{x}) and nonzero control inputs (\underline{u}). Furthermore, the costs are assumed to be quadratic in nature, that is, the cost is proportional to the weighted squares of the states and/or control inputs. Maybeck [25:10] defines a simple form of quadratic cost function as:

$$J = \mathcal{E} \left[\sum_{i=0}^N \frac{1}{2} \left[\underline{x}^T(t_i) \mathbf{X}(t_i) \underline{x}(t_i) + \underline{u}^T(t_i) \mathbf{U}(t_i) \underline{u}(t_i) \right] + \frac{1}{2} \underline{x}^T(t_{N+1}) \mathbf{X}_f \underline{x}(t_{N+1}) \right] \quad (2.41)$$

where t_0 and t_{N+1} are the start and final times, respectively. The i and N are time indices here and should not be confused with their use as mode indices in Zernike functions. A more general cost function includes cross terms between states and control inputs [25:73], but this extension is not used here.

The design of the LQG regulator involves determining the optimal input voltages to

the mirror, $\underline{u}^*(t_i)$, which minimizes the right-hand side of Equation (2.41). Minimization of this cost must be related to minimization of the phase distortion in the image reflected from the deformable mirror (maximizing performance). This relationship is implemented via the weighting matrices $X(t_i)$, $U(t_i)$, and X_f .

Since only noise-corrupted measurements are available, a Kalman filter is used to estimate the states (\underline{x}) given the measurements. Figure 2.7 shows a block diagram of a generic LQG controller. In the context of the adaptive optics control of this research, the $\underline{z}(t_i)$ are the discrete-time measurements from a Hartmann slope sensor, and the $\underline{u}(t_i)$ are the mirror control voltages.

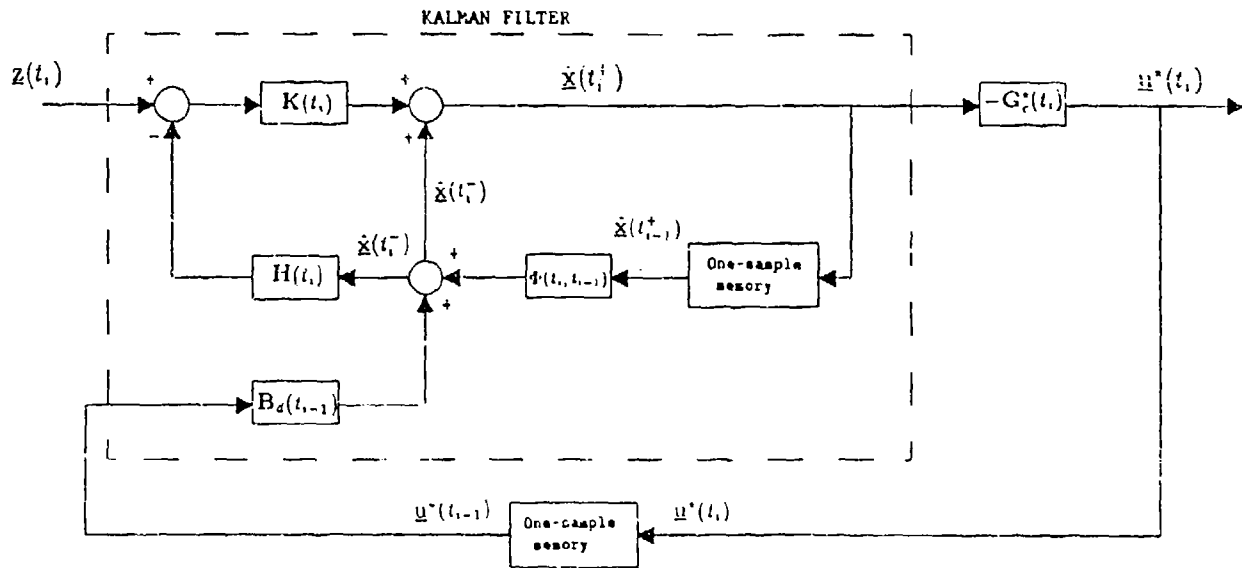


Figure 2.7. Block Diagram of LQG Controller

2.4.1 Kalman Filter The Kalman filter for the simple LQG controller can be designed separately from the regulator due to the certainty equivalence principle [25:17]. The Kalman filter accepts as inputs the measurements $\underline{z}(t_i)$ and generates an estimate of the system state, $\hat{\underline{x}}(t_i)$. It accomplishes this by using an internal model of the system to

propagate this state estimate and its covariance, P , and then updating its estimate by appropriate processing of measurements. The filter covariance is:

$$P = E\{[\underline{x} - \hat{\underline{x}}][\underline{x} - \hat{\underline{x}}]^T\} \quad (2.42)$$

As will be seen shortly, in a Kalman filter: this covariance is not dependent on the actual values of the measurements.

Kalman filter operation can be divided into two sequential processes involving the filter state estimate and covariance: propagation and measurement update. Propagation is the change in the state estimate and filter covariance as measurement-free time elapses. The measurement update process is the change in the state estimate and filter covariance as a set of measurements is processed. The governing equations are [25:18-19]:

$$\hat{\underline{x}}(t_i^-) = \Phi(t_i - t_{i-1})\hat{\underline{x}}(t_{i-1}^+) + B_d \underline{u}(t_{i-1}) \quad (2.43)$$

$$P(t_i^-) = \Phi(t_i - t_{i-1})P(t_{i-1}^+)\Phi^T(t_i - t_{i-1}) + G_d Q_d G_d^T \quad (2.44)$$

$$K(t_i) = P(t_i^-)H^T [HP(t_i^-)H^T + R]^{-1} \quad (2.45)$$

$$\hat{\underline{x}}(t_i^+) = \hat{\underline{x}}(t_i^-) + K(t_i) [\underline{z}_i - H\hat{\underline{x}}(t_i^-)] \quad (2.46)$$

$$P(t_i^+) = P(t_i^-) - K(t_i)HP(t_i^-) \quad (2.47)$$

where

| | | |
|----------------------------------|---|---|
| $\hat{\underline{x}}(t_{i-1}^+)$ | = | estimate of \underline{x} at start of $t_{i-1} \rightarrow t_i$ propagation cycle |
| $P(t_{i-1}^+)$ | = | filter covariance at start of $t_{i-1} \rightarrow t_i$ propagation cycle |
| $\hat{\underline{x}}(t_i^-)$ | = | estimate of \underline{x} at end of propagation cycle at time t_i |
| $P(t_i^-)$ | = | filter covariance at end of propagation cycle at time t_i |
| $K(t_i)$ | = | Kalman filter gain at update time |
| \underline{z}_i | = | measurement realization at update time |
| $\hat{\underline{x}}(t_i^+)$ | = | estimate of \underline{x} just after update |
| $P(t_i^+)$ | = | filter covariance just after update |

The Kalman filter gain equation implies an on-line inversion of an $m \times m$ matrix. If the number of measurements is greater than the number of states ($m > n$) then an

alternative measurement update may be preferred [26:54]:

$$\mathbf{P}(t_i^-) = \left[\mathbf{P}^{-1}(t_i^-) + \mathbf{H}^T \mathbf{R}^{-1} \mathbf{H} \right]^{-1} \quad (2.48)$$

$$\mathbf{K}(t_i) = \mathbf{P}(t_i^-) \mathbf{H}^T \mathbf{R}^{-1} \quad (2.49)$$

This form implies on-line inversions of matrices having dimensions of $n \times n$.

2.4.2 Linear Quadratic Regulation As derived by Maybeck [25] using a dynamic programming approach, the optimal control input can be written as:

$$\underline{u}^* (\hat{\underline{x}}(t_i^+), t_i) = -\mathbf{G}_c^*(t_i) \hat{\underline{x}}(t_i^+) \quad (2.50)$$

Assuming time-invariant cost matrices, the optimal controller gain $\mathbf{G}_c^*(t_i)$ is :

$$\mathbf{G}_c^*(t_i) = \left[\mathbf{U} + \mathbf{B}_d^T \mathbf{K}_c(t_{i+1}) \mathbf{B}_d \right]^{-1} \mathbf{B}_d^T \mathbf{K}_c(t_{i+1}) \Phi(t_{i+1} - t_i) \quad (2.51)$$

where the controller Riccati matrix $\mathbf{K}_c(t_i)$ is propagated via the backward Riccati difference equation [25:15]:

$$\begin{aligned} \mathbf{K}_c(t_i) = & \mathbf{X} + \Phi^T(t_{i+1} - t_i) \mathbf{K}_c(t_{i+1}) \Phi(t_{i+1} - t_i) \\ & - \Phi^T(t_{i+1} - t_i) \mathbf{K}_c(t_{i+1}) \mathbf{B}_d \left[\mathbf{U} + \mathbf{B}_d^T \mathbf{K}_c(t_{i+1}) \mathbf{B}_d \right]^{-1} \\ & \times \mathbf{B}_d^T \mathbf{K}_c(t_{i+1}) \Phi(t_{i+1} - t_i) \end{aligned} \quad (2.52)$$

from the terminal condition:

$$\mathbf{K}_c(t_{N+1}) = \mathbf{X}_f \quad (2.53)$$

This backward Riccati equation generally exhibits a terminal transient as t_{N+1} is approached. If the system is never expected to reach the terminal condition, i.e., if $t_{N+1} = \infty$, then the steady-state solution to the backward Riccati equation can be used for \mathbf{K}_c for all bounded time. Substituting this \mathbf{K}_c into Equation (2.51) yields the steady-state controller gain \mathbf{G}_c^* .

2.5 Summary

Light traveling through atmospheric turbulence is subject to spatial and temporal variations in index of refraction along the propagation path. These variations result in phase distortions in formed images. The statistics of such distortions are dependent on temporal and spatial characteristics of the atmosphere. The structure function expresses the random nature of some of these statistics, and is the foundation upon which much of the literature builds.

A quantitative description of the phase distortion in an image can be expressed as an infinite sum of weighted Zernike basis functions. That the phase distortion is not necessarily time invariant is expressed in the time-dependency of the Zernike coefficients.

Linear Quadratic Gaussian (LQG) control is one approach to controlling a dynamic system. Such a system is expressed in state-space form as a set of linear dynamics equations and a set of linear measurement equations. LQG control utilizes estimates of the system state to derive a set of control inputs, the goal being minimization of a cost function. For the adaptive optics system, the phase distortion in an image reflected from a deformable mirror is to be minimized.

III. Stochastic Models

3.1 Adaptive Optics System

The adaptive optics system of interest is a ground-based telescope which is used to observe artificial earth satellites. It is assumed that a monochromatic, coherent source of 514-nm light is within the same isoplanatic patch. It is also assumed that the light intensity is of sufficient strength to be seen against background light. A simplified schematic of the adaptive optics system is shown in Figure 3.1. The key components to be modeled and/or designed are:

1. Atmospheric distortion
2. Deformable mirror
3. Wavefront sensor
4. Kalman filter
5. Controller

The development which follows treats these topics in the order indicated. The overall system states will consist of the atmospheric distortion Zernike coefficients augmented with the Zernike coefficients corresponding to the mirror shape.

3.2 Atmospheric Effects

Based on Taylor's frozen turbulence concept introduced in Section 2.1.3, the temporal statistics of image distortion can be modeled as the spatial statistics "blowing by." A common analytical way of implementing these temporal statistics is to let the phase front distortion in the receiving aperture be modeled using Zernike basis functions, and let the Zernike coefficients (i.e. the elements of $\underline{a}_a(t)$ where the subscript a denotes atmosphere) be outputs of shaping filters. [16]. According to Noll [29:210], these Zernike coefficients are well-modeled as zero-mean Gaussian random processes. Gaussianness results from the summation of the distortions from each atmospheric layer of turbulence traversed. The turbulence of each layer contributes a random increment to the final set of Zernike

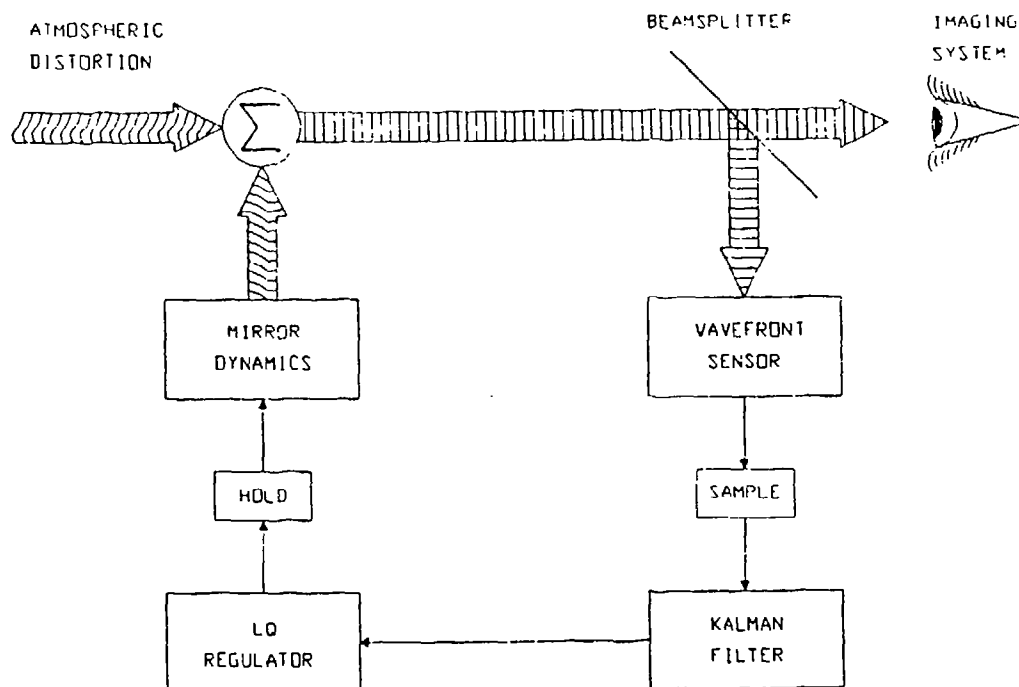


Figure 3.1. Simple Schematic of Adaptive Optics LQG Control

coefficients of phase distortion. The central limit theorem states that the sum of many such independent random contributions is Gaussian.

The general equations describing the atmospheric distortion shaping filters are of the form:

$$\dot{\underline{x}}_a(t) = \mathbf{F}_a \underline{x}_a(t) + \mathbf{G}_a \underline{w}_a(t) \quad (3.1)$$

The \mathbf{F}_a , \mathbf{G}_a , and \mathbf{Q}_a are modeled in this research as time invariant. Absence of a $\mathbf{B}_a \underline{u}(t)$ term is due to the atmospheric distortion being uncontrollable. The dimension of $\underline{x}_a(t)$ will in general be greater than the number of Zernike modes modeled, since each Zernike

coefficient may require multiple shaping filter states.

For this research atmospheric distortion is modeled as consisting of Zernike modes 1-14. The processes $\underline{a}_a(t)$ corresponding to these 14 coefficients can be extracted from the total distortion state vector $\underline{x}_a(t)$ via multiplication by an extraction matrix \mathbf{A} :

$$\underline{a}_a(t) = \mathbf{A}\underline{x}_a(t) \quad (3.2)$$

The vector $\underline{a}_a(t)$ denotes the Zernike coefficients of the image phase distortion (excluding piston) entering the adaptive optics system.

One means of designing atmospheric distortion shaping filters (i.e. \mathbf{F}_a , \mathbf{G}_a and \mathbf{Q}_a) would be to plot actual power spectral density (PSD) data for each Zernike coefficient, based on collected data. For added authenticity, the data could be collected using ground-based sensors at the actual telescope site. Having the PSDs plotted, straight-line approximations could be drawn to determine corner frequencies and strengths of shaping filter driving noise. Actual PSD data is unavailable for this research, but does exist [23]. Glasson and Guha [10:13] use this approach to model the phase distortion due to atmospheric turbulence for the first five Zernike modes. They accomplish this modeling by fitting a series of straight lines to simulated power spectral density data.

Another approach for designing the atmospheric distortion shaping filters is to simulate the Zernike coefficients' autocorrelation kernels from analytically-derived equations, followed by curve-fitting to standard shaping-filter equations. Derivation of the required analytical relations is beyond the scope of this research, as Section 2.1.4 points out. Appendix D presents the details of generating the simulated autocorrelation kernel data and the use of curve-fitting the data to shaping filter functions. Also presented in Appendix D are the matrices \mathbf{F}_a , and \mathbf{Q}_a of Equation (3.1) as well as the extraction matrix \mathbf{A} of Equation (3.2). The software developed to generate simulated autocorrelation data is archived at AFIT [39].

3.3 Mirror

This research assumes the mirror is a monolithic deformable mirror with 129 (97 active) evenly-spaced actuators, manufactured by Itek. A sample of this mirror is at the optics laboratory at the AFWL. The mirror consists of four major components: facesheet, base, electronic circuitry, and actuators. The facesheet is a monolithic piece of ultra-low expansion glass (ULE). The 129 actuator pusher pads are precisely machined into the back side of the facesheet. The base is made of similar ULE to minimize any relative thermal expansion effects, i.e., lateral forces on the actuators [21:1].

Each of the 129 piezoelectric actuators is constructed from layers of lead magnesium niobate (PMN). Each actuator is epoxied to both the facesheet and the base. The actuators are electrorestrictive, meaning either a positive or negative voltage causes the actuator to contract, i.e., the piezoelectric stack to "shorten." To make two-way excursions of the actuator possible, the stack is biased to -150 volts. Thus, application of a positive voltage reduces the total voltage magnitude, causing the stack to expand. Application of a negative voltage increases the total voltage magnitude, causing the stack to contract. The maximum magnitude of applied voltage allowed is 300 volts [21:1].

Application of these large voltages to the actuators is controlled by a control voltage whose range is ± 10 volts. A -10 volt control voltage corresponds to -150 volts applied; making the total voltage magnitude 300 volts. A +10 volt control voltage corresponds to +150 volts applied, making the total voltage magnitude 0 volts. Thus, positive control voltage causes the stack to expand; negative control voltage causes it to contract [21:1].

Of the 129 actuators on the mirror, only the central 97 are actively controllable. The Itek Operation Manual [21:4] states the remaining 32 could be made independently controllable by the addition of respective driver electronics. At present, these extras are tied to a bias voltage to provide fixed boundary conditions. Figure 3.2 shows the location and numbering scheme for the 97 active actuators, assuming the manufacturer-specified 0.85-cm spacing.

It should be noted that the configuration of this mirror at the AFWL optics development laboratory has only the central 69 actuators independently controlled; the remaining

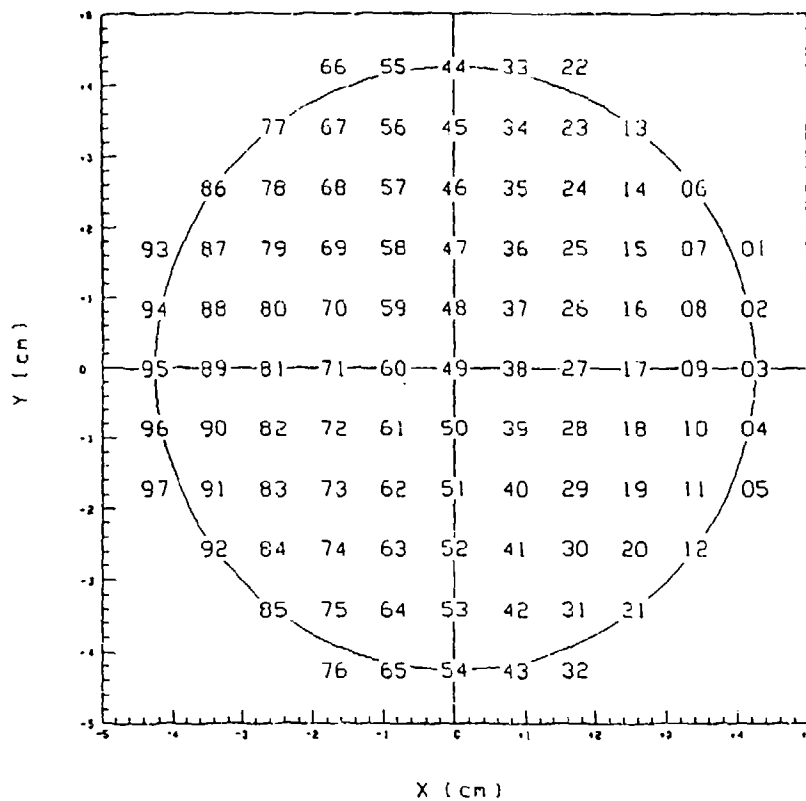


Figure 3.2. Actuator Locations on Itek 97-Actuator Mirror

28 are slaved to the nearest neighbor within the central 69 [23]. This arrangement is used to implement the so-called "zonal" approach to mirror control in which each actuator corresponds to a spatial sample of the image in the measurement device. In this case, the Hartmann wavefront sensor (to be discussed in Section 3.5) has 69 subapertures. This research, however, uses the so-called "modal" approach, which implies control of (Zernike) modes of the distortion. Greenwood [11:549] states, without justification, that the degrees of correction possible with either approach are similar. He further states the current (1978) preference is the zonal approach. Southwell [35:1006], on the other hand, argues that reconstruction of the phasefront from Hartmann-type sensor measurements appears to be superior for the modal approach. This research will not compare one approach to the other; the zonal approach is merely mentioned to explain the AFWL configuration. This research assumes all 97 active actuators are driven.

The mirrored surface of the facesheet in front of the 97 actuators lies within a 4.25-cm radius opening in a circular bezel. Thus the effective diameter of the mirror aperture is 8.5 cm. Table 3.1, condensed from the Itek Operation Manual [21:6], shows additional mirror parameters.

Table 3.1. AFWL Deformable Mirror Characteristics

| | |
|-----------------------|----------------------------------|
| Facesheet material | ULE |
| Clear aperture | 8.5 cm |
| Number of actuators | 97 controlled + 32 biased |
| Actuator geometry | Square array, 11 across diameter |
| Actuator spacing | 0.85 cm |
| Hysteresis | None observed |
| Stroke | 3.91 microns (mean) |
| Surface figure | $\lambda/10$ p-p @ 0.6328μ |
| Coating | Protected aluminum |
| Reflectivity | >84% |
| Actuator bandwidth | 500 Hz |
| Operating temperature | 20°C-30°C |
| Package size | 12-inch cube |

Linearity of a *single* actuator implies that the graph of local mirror displacement versus control voltage is a straight line. AFWL performed such measurements on a few actuators; one of their plots is shown in Figure 3.3 [22]. Because of the flattening at the ends of the control voltage range, the behavior is not strictly linear. However, over a reasonable range of control voltage, the function is approximately linear. The design of the controller assumes a linear model. It is expected that an appropriate weighting matrix in the cost function will keep the control voltage within the linear range most of the time.

Linearity of the *collection* of actuators implies inter-actuator superposition holds. For example, applying one control volt to actuator # 39, measuring the mirror response, then applying one control volt to actuator # 59, and adding the responses should yield the same

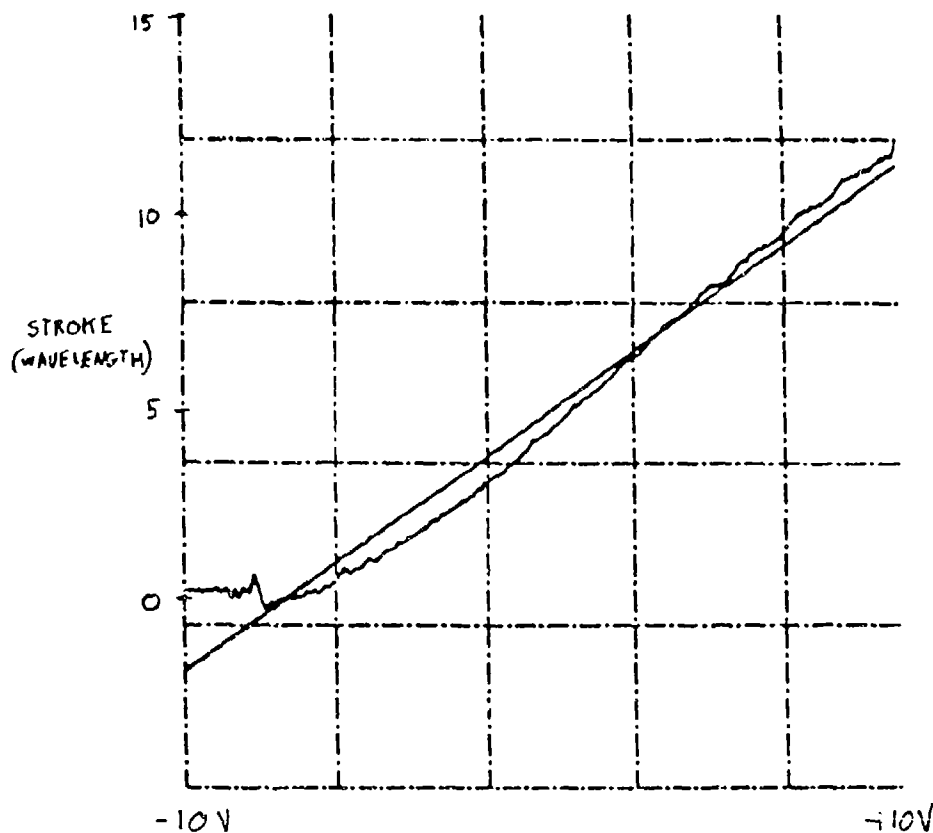


Figure 3.3. Sketch of Actuator Displacement Linearity

total response as applying the voltages simultaneously. Such multi-actuator measurement data are not available for this mirror, but this research will assume superposition holds. The literature contains precedent for the validity of the superposition assumption [1:31].

3.3.1 Steady-State Mirror Behavior It is expected and desired that application of a control voltage to an actuator will cause the mirror to deform. This deformation, however, does not occur instantaneously; a finite time is required for the mirror to attain its "steady-state" position. This section of the report addresses the relationship between applied control voltage and the steady-state mirror response. The eventual goal is to relate a vector of 97 control voltages to a vector of 14 resulting Zernike coefficients. These "mirror" Zernike coefficients add to the 14 "atmospheric" Zernike coefficients of the incident atmosphere-aberrated light, hopefully cancelling them. Thus, reflection from the deformable mirror is modeled as the addition of atmospheric Zernike coefficients to the mirror Zernike coefficients.

The *influence function* is a mathematical representation of the effect of a single actuator voltage on the local mirror shape. Usually, the influence function is nonzero only in the vicinity of the actuator: the influence function of an actuator has a limited spatial domain. Several factors affect the influence function of an actuator. These factors include piezoelectric type, facesheet material and thickness, proximity and geometry of neighboring actuators, and actuator linearity. Based on the previous assumptions of actuator linearity and evenly-spaced geometry, it is assumed that all actuators have the same influence function. The fact that the word "mean" appears in Table 3.1 for the actuator stroke parameter implies that each actuator does not have the same influence function. Nevertheless, this research assumes uniformity of the 97 influence functions.

Limited influence data is available for the Itek mirror at the AFWL. Itek provided data corresponding to a two-dimensional slice of the influence function for the central actuator, #49. This slice was taken along the mirror X-axis, spanning actuators 71, 60, 49, 38, and 27. Itek's plot of this data is shown in Figure 3.4. The magnitude of the voltage applied to the actuator was 200 volts for this data. Influence data was also available along a 45-degree slice through the central actuator. This data showed less of a negative excursion, but was of the same general shape as the slice along the X-axis. Thus, it is assumed that the slice through the X-axis is approximately valid in any direction. The ordinate data (X) used to plot Figure 3.4 were converted into units of cm. The abscissa data were converted into 2-way decrease in path length, measured in wavelengths of 514-nm light. The abscissa data were then scaled to represent one volt of control voltage, invoking the linearity assumption. The transformed data were curve-fit to a tenth-order polynomial in X truncated at $X = \pm 1.6739$ cm, the spatial domain of influence. The truncated function was then rotated about the actuator axis (i.e., the "Z" axis) resulting in the three dimensional influence function of the central actuator. This influence function, when expressed in mirror coordinates, yields:

$$\begin{aligned}
 f(X, Y, X_A, Y_A) = & \{0.9673 \\
 & -2.726 [(X - X_A)^2 + (Y - Y_A)^2] \\
 & + 2.943 [(X - X_A)^2 + (Y - Y_A)^2]^2
 \end{aligned} \tag{3.3}$$

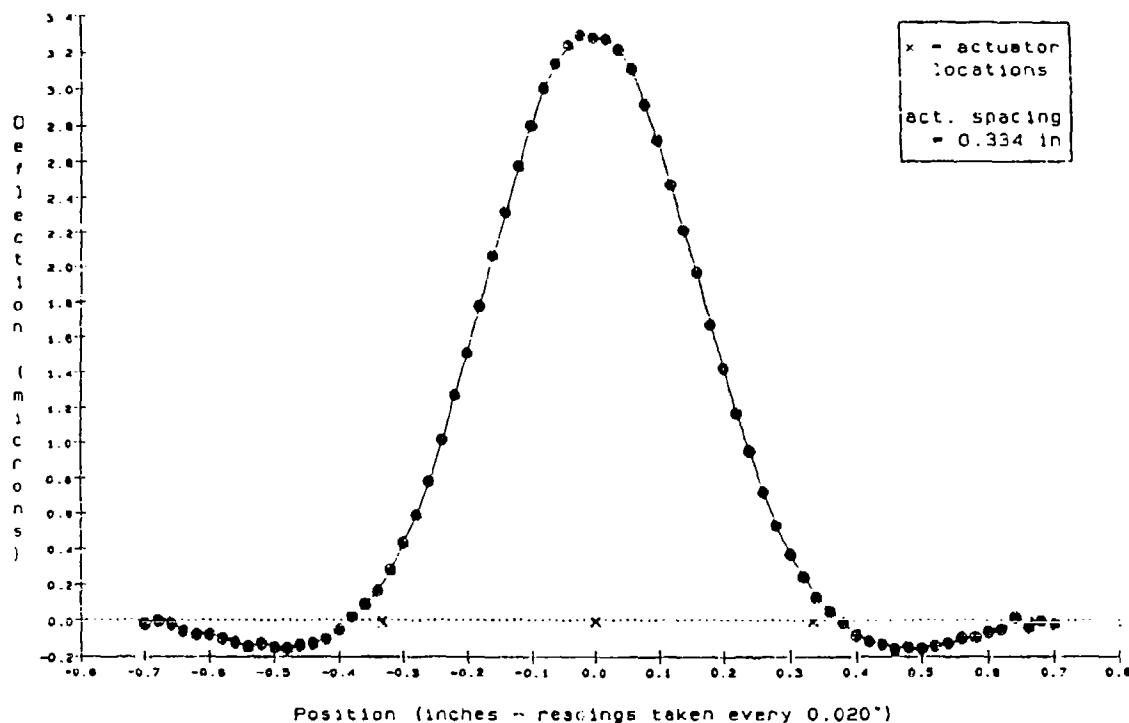


Figure 3.4. X-Axis Slice of Actuator #49 Influence Function

$$\begin{aligned}
 & -1.573 \left[(X - X_A)^2 + (Y - Y_A)^2 \right]^3 \\
 & + 0.4137 \left[(X - X_A)^2 + (Y - Y_A)^2 \right]^4 \\
 & - 0.04236 \left[(X - X_A)^2 + (Y - Y_A)^2 \right]^5 \} \\
 & \times \left\{ u_{-1} \left([1.6739]^2 - [(X - X_A)^2 + (Y - Y_A)^2] \right) \right\} \quad (3.4)
 \end{aligned}$$

where

X, Y = coordinates of point on mirror (cm)
 X_A, Y_A = coordinates of actuator (cm)
 $u_{-1}(\cdot)$ = unit step function
 f = 2-way path-length decrease (wavelength/volt)

Figure 3.5 shows the three-dimensional plot of the influence function for the central actuator. Note the X,Y units are cm, whereas the "Z" units are wavelengths. This accounts for the extreme protruding appearance of the plot.

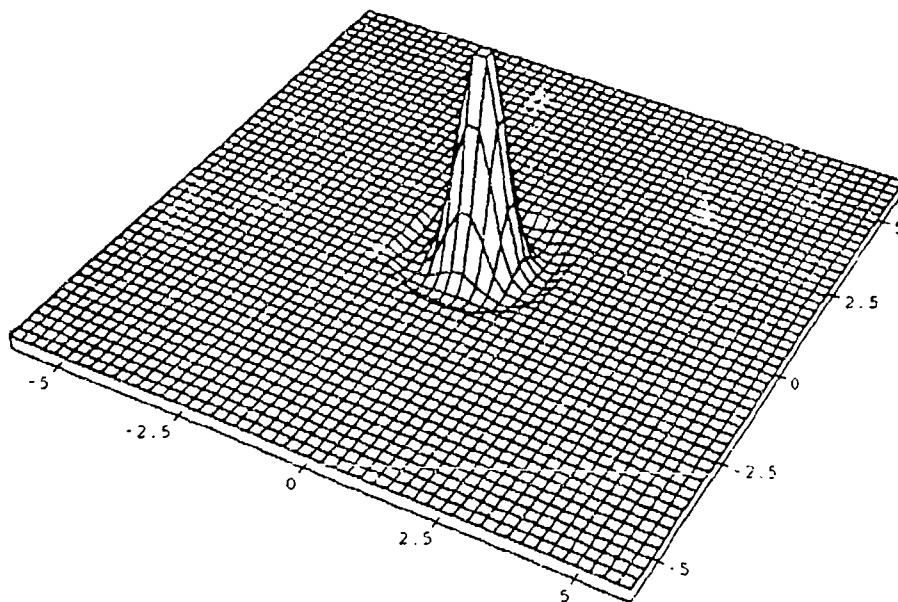


Figure 3.5. Approximate Influence Function for Actuator #49

At this point, a mental example is helpful. Suppose a perfectly planar wavefront is incident on the mirror. Further, suppose that one volt of control voltage is applied to an arbitrary actuator, all other control voltages being zero. Let the X,Y position of interest be right at the actuator, i.e., $X = X_A$ and $Y = Y_A$. Therefore, the value of f at that actuator is 0.9673 wavelengths. Actually, the mirror only moves 0.4836 wavelengths at the actuator, but this causes the path-length of the reflected light to be reduced by twice as much and f is defined to be such reduction in path length. Suppose the light reflected from the entire mirror then passes through an aperture of the same diameter. The light in this aperture corresponding to that reflected from the extended actuator reaches the aperture first since its path length is shorter. Thus, its absolute phase is a larger value than that of the light from the rest of the mirror. Therefore, a plot of the phase deviation

in the aperture looks exactly like the influence function plot with piston subtracted out.

The previous discussion can be extended to the case where control voltages are applied to all 97 actuators. Assume that the light incident on the mirror is perfectly planar. Thus any phase distortion in the reflected image will be solely due to the mirror shape. All 97 actuators are then excited by arbitrary but time-invariant control voltages. When the mirror's shape reaches steady state, a snapshot of the phase distortion in the *reflected* image can be obtained by subtracting the spatial-average phase (i.e., the piston). An appropriate equation for the phase distortion in the reflected image is:

$$\phi(X, Y) = \left[\sum_{A=1}^{97} f(X, Y, X_A, Y_A) u(A) \right] - \epsilon \left[\sum_{A=1}^{97} f(X, Y, X_A, Y_A) u(A) \right] \quad (3.5)$$

Equation (3.5) represents the mirror's contribution to the distortion of the reflected image. Since the left-hand side is phase deviation in an aperture, it can be expressed as a linear combination of Zernike functions Z_1 through Z_∞ . For this research, the atmospheric distortion is modeled as the first 14 of these. It then follows the mirror will only be trying to correct only the first 14 modes. Thus the significant phase deviation caused by some *operational* set of commands to the mirror can be modeled as linear combinations of the first 14 Zernike functions (as usual, excluding piston):

$$\phi(X, Y) \approx \sum_{i=1}^{14} a_i Z_i(X, Y) \quad (3.6)$$

The a_i Zernike coefficients can be determined using Equation (2.25), expressed below in rectangular form:

$$a_i = \frac{\int dY \int dX W(X, Y) \phi(X, Y) Z_i(X, Y)}{\int dY \int dX W(X, Y)} \quad (3.7)$$

Substituting Equation (3.5) into Equation (3.7), and realizing that the product of piston and any non-piston Zernike function integrates to zero yields:

$$a_i = \frac{\int dY \int dX W(X, Y) \left[\sum_{A=1}^{97} f(X, Y, X_A, Y_A) u(A) \right] Z_i(X, Y)}{\int dY \int dX W(X, Y)} \quad (3.8)$$

One can then pull the summation outside the integrals, and commute the scalar control voltage:

$$a_i = \sum_{A=1}^{97} \left\{ \left[\frac{\int dY \int dX W(X,Y) f(X,Y,X_A,Y_A) Z_i(X,Y)}{\int dY \int dX W(X,Y)} \right] [u(A)] \right\} \quad (3.9)$$

Equation (3.9) can be expressed in vector form:

$$a_i = \underline{m}_i^T \underline{u} \quad (3.10)$$

where the A-th component of the \underline{m} vector is the projection of the A-th actuator's influence function along the i-th Zernike function. Likewise the A-th component of the \underline{u} vector is the control voltage on the A-th actuator. Equation (3.10) can be written for each Zernike function:

$$\begin{aligned} a_1 &= \underline{m}_1^T \underline{u} \\ a_2 &= \underline{m}_2^T \underline{u} \\ &\vdots \\ a_{14} &= \underline{m}_{14}^T \underline{u} \end{aligned} \quad (3.11)$$

Finally, Equations (3.12) can be combined into matrix form as:

$$\underline{a} = \underline{M} \underline{u} \quad (3.12)$$

where \underline{a} is the vector of Zernike coefficients describing the mirror's *steady-state* contribution to the distortion of the reflected image. The matrix \underline{M} is the steady-state influence matrix, since it relates the steady-state influence of the mirror to the applied control voltages. Each element of the matrix is the projection of an actuator's influence function along a Zernike function direction. The Fortran program which calculates the \underline{M} matrix for this research is archived at AFIT [39]. The resulting \underline{M} matrix is shown in Appendix E.

In order to check the reasonableness of the steady-state influence matrix, it was decided to perform a test. The test consisted of analytically determining the required

control voltage vector to cause the reflected image to consist of a selected Zernike mode, assuming perfectly planar incident light. Then the resulting voltage vector was applied to the mirror in a mathematical simulation to see if the resulting phase deviation plot "looked like" a plot of the selected Zernike function. The 14-th Zernike function was selected because of its high spatial frequency content relative to the other modes. If the mirror is able to reproduce the 14-th mode well, it should be able to reproduce lower-order modes as well. An arbitrary value of a_{14} was chosen, with the remaining coefficients set to zero. Equation (3.12) was then solved for the required voltage vector[14:35]:

$$\underline{u} = \mathbf{M}^T (\mathbf{M} \mathbf{M}^T)^{-1} \underline{a} \quad (3.13)$$

This is the unweighted, minimum-norm solution. This series of matrix and vector operations resulted in a set of 97 control voltages. A Fortran program was then used to simulate the phase deviation caused by the set of voltages and generate plotable results. Comparison of Figure 3.6 with the plot of the 14-th Zernike function in Appendix A lends credibility to the calculated \mathbf{M} matrix.

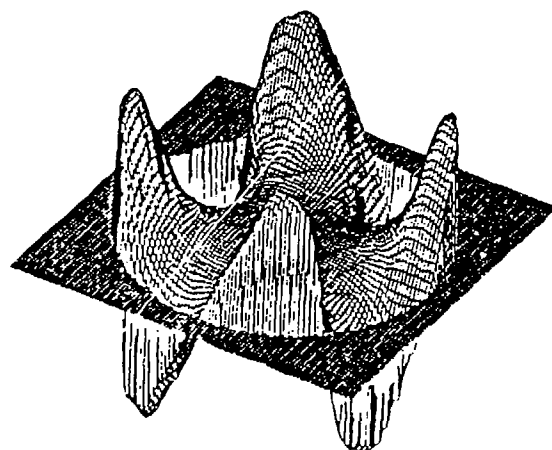


Figure 3.6. Simulated Mirror Reconstruction of 14-th Zernike Mode Phase Distortion

3.3.2 *Transient Behavior* Up until now, only the steady-state behavior of the mirror has been considered; the mirror has been given time to respond completely to the input

control voltages. Now the transient behavior of the mirror will be considered. The mirror's manufacturer description states that an actuator acts as a electrical capacitive load [21]. It is thus reasonable to expect that application of a step control voltage to an actuator does not result in a step response, but rather, an exponential approach to an asymptote.

The Operation Manual [21:6] for the Itek deformable mirror indicates the mean bandwidth for the actuators is 500 Hz. AFWL bandwidth data [22] is generally in agreement. Figure 3.7 is the AFWL plot of the frequency response for one of the 97 active channels. For this particular actuator channel, the -3-dB frequency is 497 Hz. It is assumed this

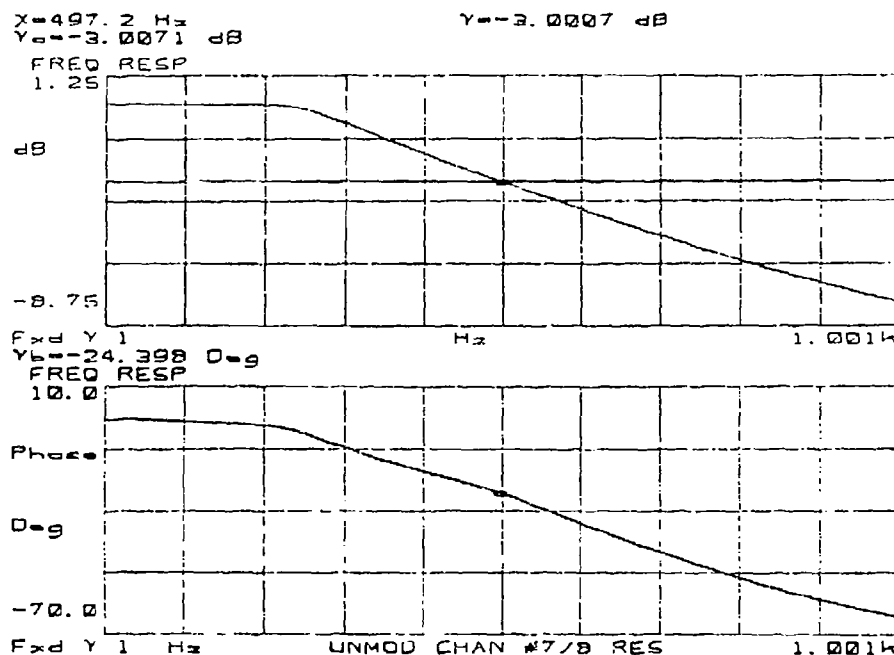


Figure 3.7. Frequency Response of An AFWL Mirror Actuator Channel

plot includes the effects of the driver circuitry dynamics and the mirror dynamics. The approximate slope of the rolloff is -10 dB per decade of frequency, which confirms the presence of a first order pole. It is assumed the decibel values plotted are normalized with respect to the low frequency response:

$$\# \text{ of dB} = 10 \log \left[\frac{R(f)^2}{R(0)^2} \right] \quad (3.14)$$

where R is the ratio of sinusoidal excitation magnitude to sinusoidal response magnitude. Assuming the dynamics of the mirror are first order, time-invariant, and deterministic, the dynamics equation for the displacement at the actuator site for control-voltage excitation of the actuator can be modeled by the scalar dynamics equation:

$$\dot{g}(t) = c g(t) + d u(t) \quad (3.15)$$

where g is the decrease in 2-way path-length of light reflected at the actuator (i.e., twice the actual physical displacement of the mirror at the actuator site). The values of c and d in Equation (3.15) will now be analytically determined, using the bandwidth value and the peak displacement of the assumed influence function, Equation (3.4). Taking the Laplace transform of Equation (3.15) for zero initial displacement and rearranging yields:

$$G(s) = \frac{d}{s - c} U(s) \quad (3.16)$$

The s is the Laplace complex variable. Now if the control voltage input is switched from zero to a sinusoidal voltage at time $t=0$, the input Laplace transform can be found from a one-sided Laplace transform table [8:772]:

$$u(t) = \sin \omega t, \quad t > 0 \quad (3.17)$$

$$U(s) = \frac{\omega}{s^2 + \omega^2} \quad (3.18)$$

Substituting this into Equation (3.16) and again referring to a Laplace transform table [8:772] the time-domain response can be obtained:

$$g(t) = (d)(\omega) \left(\frac{e^{ct}}{c^2 + \omega^2} + \frac{1}{\omega \sqrt{c^2 + \omega^2}} \sin \left(\omega t - \tan^{-1} \left[\frac{\omega}{-c} \right] \right) \right), \quad t > 0 \quad (3.19)$$

Since $c < 0$, the exponential term in the above equation vanishes as $t \rightarrow \infty$. Thus, after the transient response has died out, the sinusoidal "steady-state" response is:

$$g_{ss}(t) = \frac{d}{\sqrt{c^2 + \omega^2}} \sin \left(\omega t - \tan^{-1} \left[\frac{\omega}{-c} \right] \right), \quad t > 0 \quad (3.20)$$

At zero frequency, the amplitude of g is merely $\frac{d}{c}$. At the bandwidth frequency (assumed to be 500 Hz, or 1000π rad/sec), the amplitude of g should be $\frac{1}{\sqrt{2}} \frac{d}{c}$. Therefore the equation

$$\frac{1}{\sqrt{2}} \frac{d}{c} = \frac{d}{\sqrt{c^2 + (1000\pi)^2}} \quad (3.21)$$

can be solved for c , yielding :

$$\begin{aligned} c &= -\frac{1000\pi}{\sqrt{2}} \text{ sec}^{-1} \\ &\approx -2222 \text{ sec}^{-1} \\ &\approx -\frac{1}{0.00045 \text{ sec}} \end{aligned} \quad (3.22)$$

Thus it can be said the time constant of a typical actuator is approximately 0.45 milliseconds.

From Equation (3.4) the steady-state value of g for a unit step control voltage $u(t)$ is 0.9673 wavelengths. The left-hand side of Equation (3.15) is zero at steady-state for a step input. With zero on the left-hand side and $u_{ss}(t)$ set equal to one, Equation (3.15) can be solved for d . The resulting value for d is:

$$\begin{aligned} d &= \frac{-c g_{ss}(t)}{u_{ss}(t)} \\ &= \frac{-\left(-\frac{1000\pi}{\sqrt{2}}\right) g_{ss}(t)}{u_{ss}(t)} \\ &= \frac{-\left(-\frac{1000\pi}{\sqrt{2}}\right) (0.9673)}{1} \\ &\approx 2150 \frac{\text{wavelengths}}{\text{volt sec}} \end{aligned}$$

Thus the dynamics of an actuator can be approximated by:

$$\dot{g}(t) = -\frac{1}{0.00045} g(t) + 2150 u(t) \quad (3.23)$$

The validity of Equation (3.23) for any actuator obviously depends on the assumptions of all actuators having the same influence function and bandwidth. Also the dynamics

are assumed to be deterministic. With additional statistical data on the bandwidths and influence functions of all actuators, 97 versions of Equation (3.23) could be written. Also, the noise in the control voltage could be modeled, causing the addition of a stochastic term to the equations. This research assumes the deterministic Equation (3.23) is valid for all actuators.

The previous discussion of dynamics at the actuator site can be extended to the phase distortion over the entire mirror. It is desired to formulate the dynamics of the mirror in the form of:

$$\dot{\underline{x}}_m(t) = \mathbf{F}_m \underline{x}_m(t) + \mathbf{B}_m \underline{u}(t) \quad (3.24)$$

where the elements of vector $\underline{x}_m(t)$ are the time-varying Zernike coefficients which describe the mirror's contribution to the phase distortion in the reflected image. The lack of stochastic terms is an engineering assumption. The previous assumption of identical actuator bandwidths implies the entire mirror has the same bandwidth, and therefore the same time constant. If a set of 97 control voltages is simultaneously applied to the mirror, therefore, the dynamic behavior of the entire mirror surface would exhibit behavior indicative of a 0.00045-second time constant. Thus, if $\phi_m(X, Y, t)$ is the mirror's contribution to the phase distortion in the reflected image then the following scalar equation can be written:

$$\dot{\phi}_m(X, Y, t) = -\frac{1}{\tau} \phi_m(X, Y, t) + \underline{b}_m^T(X, Y) \underline{u}(t) \quad (3.25)$$

The vector of functions $\underline{b}_m(X, Y)$ maps the voltage of each actuator to the rate-of-change of phase at point (X, Y) . The phase distortion introduced by the mirror, $\phi_m(X, Y, t)$, can be approximated by a linear combination of a finite number of Zernike basis functions:

$$\phi_m(X, Y, t) \approx a_1(t)Z_1(X, Y) + a_2(t)Z_2(X, Y) + \cdots + a_{14}(t)Z_{14}(X, Y) \quad (3.26)$$

Taking the time-derivative of Equation (3.26) yields:

$$\dot{\phi}_m(X, Y, t) \approx \dot{a}_1(t)Z_1(X, Y) + \dot{a}_2(t)Z_2(X, Y) + \cdots + \dot{a}_{14}(t)Z_{14}(X, Y) \quad (3.27)$$

An immediate temptation is to write these two equations in vector form, followed by substitution into Equation (3.25), which would yield:

$$\dot{\underline{a}}(t)^T \underline{Z}(X, Y) = -\frac{1}{\tau} \underline{a}(t)^T \underline{Z}(X, Y) + \underline{b}_m^T(X, Y) \underline{u}(t) \quad (3.28)$$

To get Equation (3.28) into the form of Equation (3.24) with the Zernike coefficients being the states, one is further tempted to take the transpose of both sides of Equation (3.28), then premultiply both sides by the vector $\underline{Z}(X, Y)$, then premultiply both sides by the matrix inverse $[\underline{Z}(X, Y) \underline{Z}^T(X, Y)]^{-1}$. The problem with this approach is that $[\underline{Z}(X, Y) \underline{Z}^T(X, Y)]$ is a rank-one matrix whose inverse does not exist.

To get Equation (3.25) into the form of Equation (3.24), use is made of the orthogonality property of the Zernike functions. Substituting Equations (3.26) and (3.27) into Equation (3.25) yields:

$$\sum_{i=1}^{14} \dot{a}_i(t) Z_i(X, Y) = -\frac{1}{\tau} \sum_{i=1}^{14} a_i(t) Z_i(X, Y) + \sum_{j=1}^{97} b_j(X, Y) u_j(t) \quad (3.29)$$

Multiplication of Equation (3.29) by $Z_1(X, Y)$, then spatially integrating both sides of the equation over the area of the mirror aperture—using Equation (2.22) where appropriate—yields:

$$\dot{a}_1(t) = -\frac{1}{\tau} a_1(t) + \frac{1}{\pi R^2} \underline{\mu}_1^T \underline{u}(t) \quad (3.30)$$

The vector $\underline{\mu}_1$ is defined such that its j -th element is the projection of the function $b_j(X, Y)$ into $Z_1(X, Y)$. Multiplying Equation (3.29) by each successive Zernike function and following the integration procedure yields the set of equations:

$$\begin{aligned} \dot{a}_1(t) &= -\frac{1}{\tau} a_1(t) + \frac{1}{\pi R^2} \underline{\mu}_1^T \underline{u}(t) \\ \dot{a}_2(t) &= -\frac{1}{\tau} a_2(t) + \frac{1}{\pi R^2} \underline{\mu}_2^T \underline{u}(t) \\ &\vdots \end{aligned} \quad (3.31)$$

$$\dot{a}_{14}(t) = -\frac{1}{\tau} a_{14}(t) + \frac{1}{\pi R^2} \underline{\mu}_{14}^T \underline{u}(t) \quad (3.32)$$

Putting this set of differential equations into state-space form, yields:

$$\dot{\underline{x}}_m(t) = \text{diag} \left[-\frac{1}{\tau} \right] \underline{x}_m(t) + \underline{B}_m \underline{u}(t) \quad (3.33)$$

where $\text{diag}[\cdot]$ is a diagonal matrix of the argument and the rows of matrix \underline{B}_m are the $\underline{\mu}^T$ row vectors, divided by πR^2 .

To determine the elements of the matrix \underline{B}_m , consider the entire mirror at steady state such that $\dot{\underline{x}}_m(t) = \underline{0}$. Substituting this into Equation (3.33) and manipulation yields:

$$\underline{x}_{m,ss}(t) = \text{diag}[\tau] \underline{B}_m \underline{u}_{ss}(t) \quad (3.34)$$

Comparing this equation with Equation (3.12), it is straightforward to show that:

$$\underline{B}_{m,ss} = \text{diag} \left[\frac{1}{\tau} \right] \underline{M} \quad (3.35)$$

where \underline{M} is the steady-state influence matrix and τ is 0.00045 seconds.

In summary, the dynamics of the Itek deformable mirror are written in terms of the mirror's *contribution* to the Zernike coefficients of the reflected image. Invoking the assumptions of identical actuator influence functions and identical, first-order actuator dynamics, the equation for these contributions to the Zernike coefficients is:

$$\dot{\underline{x}}_m(t) = \text{diag} \left[-\frac{1}{\tau} \right] \underline{x}_m(t) + \text{diag} \left[\frac{1}{\tau} \right] \underline{M} \underline{u}(t) \quad (3.36)$$

It should be noted this equation is a truncation of the infinite-dimensional functional-space description to 14 dimensions.

3.4 Augmented System Dynamics

The overall continuous-time description of the adaptive optics system dynamics is:

$$\begin{bmatrix} \dot{\underline{x}}_a(t) \\ \dot{\underline{x}}_m(t) \end{bmatrix} = \begin{bmatrix} \underline{F}_a & \underline{0} \\ \underline{0} & \underline{F}_m \end{bmatrix} \begin{bmatrix} \underline{x}_a(t) \\ \underline{x}_m(t) \end{bmatrix} + \begin{bmatrix} \underline{0} \\ \underline{B}_m \end{bmatrix} \underline{u}(t) + \begin{bmatrix} \underline{w}_a(t) \\ \underline{0} \end{bmatrix} \quad (3.37)$$

The upper partition of Equation (3.37) represents atmospheric dynamics; the lower partition represents mirror dynamics.

3.5 Wavefront Sensor

The image reflected from the deformable mirror contains phase distortion due to atmospheric turbulence and also counterdistortion due to the mirror deformation. Distortion here is deviation in phase from the aperture-average phase, thus piston is excluded. Letting the phase distortion in the reflected image be modeled in the Zernike functional space, the corresponding discrete-time Zernike coefficients for the reflected image are:

$$\underline{a}(t_i) = \begin{bmatrix} \mathbf{A} & | & \mathbf{I} \end{bmatrix} \begin{bmatrix} \underline{x}_a(t_i) \\ \text{---} \\ \underline{x}_m(t_i) \end{bmatrix} \quad (3.38)$$

where \mathbf{A} is the extraction matrix defined in Equation (3.2) and \mathbf{I} is a 14-by-14 identity matrix. Note that this equation models the reflection process as a summation of two sets of Zernike coefficients. Since the wavefront sensor measures the distortion in the *reflected* image, the discrete measurement equation for the wavefront sensor can be written as:

$$\begin{aligned} \underline{z}(t_i) &= \mathbf{H}' \underline{a}(t_i) + \underline{v}(t_i) \\ &= \mathbf{H}' \begin{bmatrix} \mathbf{A} & | & \mathbf{I} \end{bmatrix} \begin{bmatrix} \underline{x}_a(t_i) \\ \text{---} \\ \underline{x}_m(t_i) \end{bmatrix} + \underline{v}(t_i) \\ &= \mathbf{H} \underline{x}(t_i) + \underline{v}(t_i) \end{aligned} \quad (3.39)$$

This research takes the approach of first calculating the \mathbf{H}' matrix analytically, then post-multiplying by the $\begin{bmatrix} \mathbf{A} & | & \mathbf{I} \end{bmatrix}$ matrix to obtain \mathbf{H} . The measurement noise covariance \mathbf{R} corresponding to $\underline{v}(t_i)$ is left as a design parameter.

3.5.1 Wavefront Sensor Description The reflected image is diverted to the wavefront sensor via a beamsplitter. Light reflected from the beamsplitter enters the Hartmann wavefront sensor. The Hartmann sensor consists of an array of square convex lenses, each

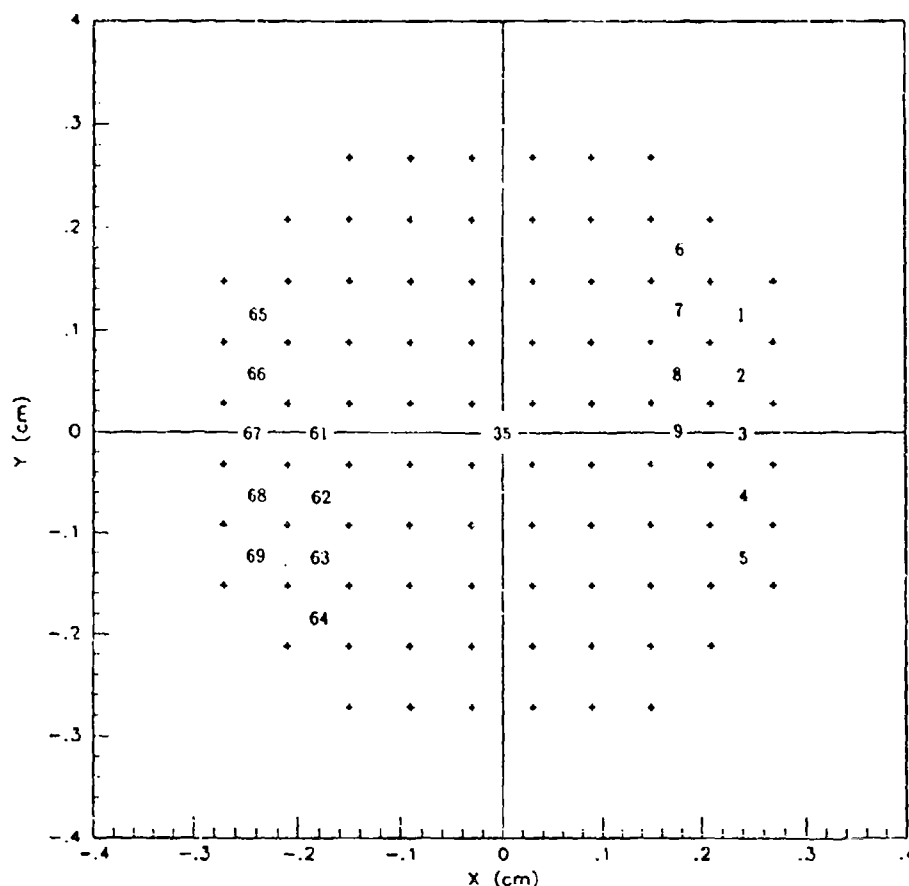


Figure 3.8. Subaperture Locations on Hartmann Wavefront Sensor

considered a subaperture of the sensor. The sensor has 69 fully-illuminated square subapertures. Figure 3.8 shows the arrangements of the subapertures in the Hartman sensor aperture. Each subaperture is 0.06 cm on a side [27] and focuses its share of the incident light onto a reticon detector. The location of the focused spot of light on the detector is an indication of the average x- and y-tilt in the subaperture. Since subaperture *tilts* are measured, the Hartmann sensor is essentially a slope sensor. Figure 3.9 shows a two-dimensional analog of the operation of the Hartmann sensor [27].

3.5.2 Derivation of H' An important concept is that phase distortion in the image manifests itself as a set of subaperture tilt measurements in the Hartmann sensor. Thus any Zernike mode (except piston) distortion of the whole image is measured as a set of tilt measurements. It is assumed the Hartmann sensor can output these 138 tilt measurements (69 x-tilts and 69 y-tilts) directly. The sensor normally processes the set of 138 tilt measurements and reconstructs the phase, but this reconstruction is based only on current tilts; previous time realizations are not considered. This reconstruction process is accom-

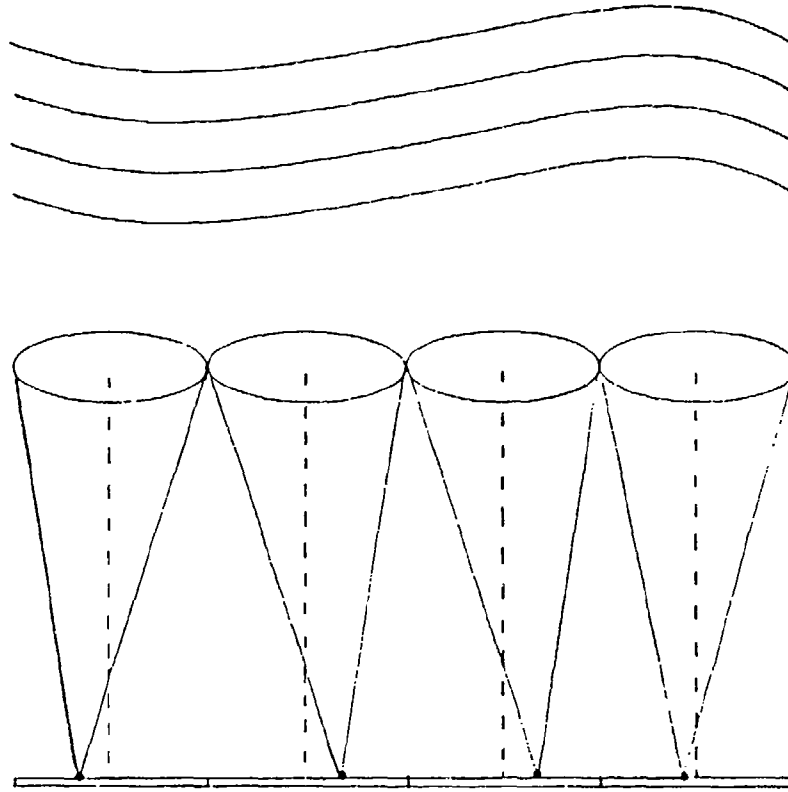


Figure 3.9. Concept of Operation for Two-Dimensional Hartmann Sensor

plished in software, requiring computational time. This research therefore assumes the 138 noise-corrupted tilt measurements are the outputs of the sensor, i.e., comprise the $\underline{z}(t_i)$ vector. The Kalman filter estimates the system states from the 138 tilt measurements.

Consider the phase distortion of the image entering the sensor to be a function of position in the aperture and discretized time:

$$\phi(X, Y, t_j) \quad (3.40)$$

The variables X and Y are rectangular coordinates with respect to the center of the total sensor aperture. Just prior to light entering one of the square subaperture lenslets, the x-tilt at position (X_1, Y_1) is:

$$\left. \frac{\partial \phi(X, Y, t_j)}{\partial Y} \right|_{X_1, Y_1} \quad (3.41)$$

Letting (X_s, Y_s) define the coordinates of the center of the s -th subaperture with respect to the entire sensor aperture, the average x-tilt going into the s -th subaperture lenslet is

then:

$$\frac{1}{A} \int_{Y_s - \frac{\sqrt{A}}{2}}^{Y_s + \frac{\sqrt{A}}{2}} dY \int_{X_s - \frac{\sqrt{A}}{2}}^{X_s + \frac{\sqrt{A}}{2}} dX \frac{\partial \phi(X, Y, t_j)}{\partial Y} \quad (3.42)$$

where A is the area of the square subaperture.

According to Petersen and Cho [32] the *output* of a Hartmann-type slope sensor is a similar integral, but with the slopes spatially weighted. For example, the output of the x-tilt channel in a subaperture (ignoring noise) is:

$$z_{x_s}(t_j) = L \frac{1}{A} \int_{Y_s - \frac{\sqrt{A}}{2}}^{Y_s + \frac{\sqrt{A}}{2}} dY \int_{X_s - \frac{\sqrt{A}}{2}}^{X_s + \frac{\sqrt{A}}{2}} dX W_x(X - X_s, Y - Y_s) \frac{\partial \phi(X, Y, t_j)}{\partial Y} \quad (3.43)$$

The constant L is dependent on wavelength, lenslet focal length, and output scaling. Petersen and Cho derive the spatial weighting function $W_x(X', Y')$ for a square subaperture; the normalized version is:

$$W_x(X', Y') = \frac{1}{2 \ln(2)} \left[2 \ln(2) - \left(1 - \frac{2Y'}{\sqrt{A}}\right) \ln \left(1 - \frac{2Y'}{\sqrt{A}}\right) - \left(1 + \frac{2Y'}{\sqrt{A}}\right) \ln \left(1 + \frac{2Y'}{\sqrt{A}}\right) \right] \quad (3.44)$$

Similar equations can be written for the subaperture y-tilt channel. A plot of Equation (3.44) for the subaperture dimensions of this research is shown in Figure 3.10. Obviously the slope of light traversing the center of the subaperture is weighted more heavily than that traversing near the edges.

If the phase distortion of an image can be represented as a linear combination of basis functions, then the partial derivative expressed in Equation (3.41) can also:

$$\frac{\partial \phi(X, Y, t_j)}{\partial Y} = a_1(t_j) \frac{\partial Z_1(X, Y)}{\partial Y} + \dots + a_{14}(t_j) \frac{\partial Z_{14}(X, Y)}{\partial Y} \quad (3.45)$$

Substitution of Equation (3.45) into Equation (3.43) and simple manipulation yields:

$$z_{x_s}(t_j) = \frac{L}{A} \sum_{i=1}^{14} \left[a_i(t_j) \int_{Y_s - \frac{\sqrt{A}}{2}}^{Y_s + \frac{\sqrt{A}}{2}} dY \int_{X_s - \frac{\sqrt{A}}{2}}^{X_s + \frac{\sqrt{A}}{2}} dX W_x(X - X_s, Y - Y_s) \frac{\partial Z_i(X, Y)}{\partial Y} \right] \quad (3.46)$$

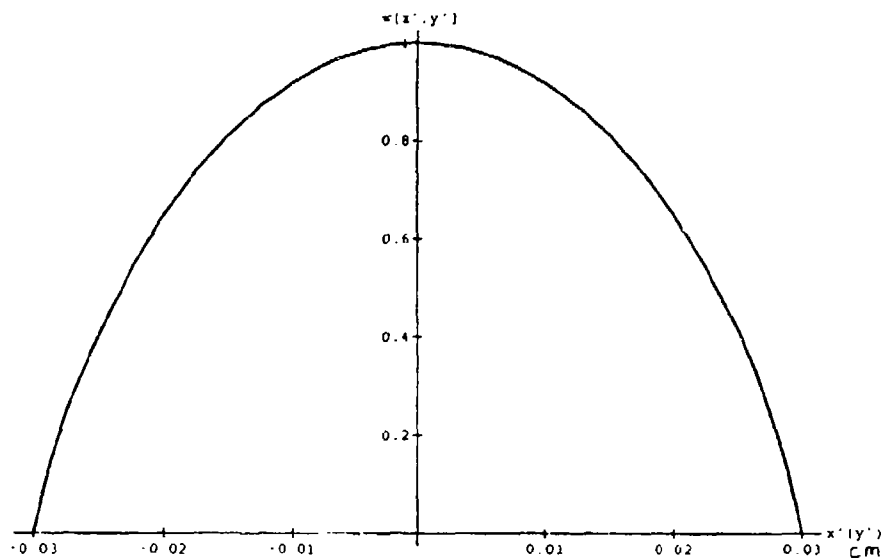


Figure 3.10. Slope Measurement Weighting Function

Equation (3.46), representing the noise-free output of the x-tilt channel for the s -th subaperture, can be written in vector notation:

$$z_{x_s}(t_j) = \frac{L}{A} \underline{n}_{x_s}^T \underline{a}(t_j) \quad (3.47)$$

The i -th element of the \underline{n}_{x_s} vector can be thought of as the projection of the i -th Zernike function into x-tilt measurement space at the s -th subaperture. Knowing the location of the center of an actuator relative to the entire aperture, and knowing the partial derivatives of the Zernike functions, the elements of \underline{n}_{x_s} can be determined as:

$$\underline{n}_{x_s,i} = \int_{Y_s - \frac{\sqrt{A}}{2}}^{Y_s + \frac{\sqrt{A}}{2}} dY \int_{X_s - \frac{\sqrt{A}}{2}}^{X_s + \frac{\sqrt{A}}{2}} dX W_x(X - X_s, Y - Y_s) \frac{\partial Z_i(X, Y)}{\partial Y} \quad (3.48)$$

Equation (3.47) can be repeated for both the x- and y-tilt channels for all 69 illuminated subapertures, continuing with the noise-free measurement assumption. The 138

resulting equations can be augmented into a matrix form:

$$\underline{z}(t_j) = \frac{L}{A} \mathbf{N} \underline{a}(t_j) \quad (3.49)$$

Therefore, the \mathbf{H}' matrix of Equation (3.39) is:

$$\mathbf{H}' = \frac{L}{A} \mathbf{N} \quad (3.50)$$

The Fortran program developed to calculate the \mathbf{N} matrix for this research is archived at AFIT [39]. Appendix F shows the resulting \mathbf{N} matrix.

To determine the value of the scaling constant, L/A , results of previous AFIT research are useful. Miller [27] collected measurement data from a realization of the Hartmann sensor studied in this research. He excited the sensor with 543.5-nm laser light and recorded the outputs from the slope channels. These outputs were not in wavelengths of tilt, but rather in internal programmable microcoded processor (PMP) units. He determined that one wavelength of tilt across a subaperture, on the average, resulted in a slope channel output of 745 PMP units. Simple algebra shows that one wavelength of y-tilt across a subaperture corresponds to the Zernike coefficient $a_1 = 2.574$. The value of L/A applicable to his research can be determined by considering the non-zero elements of the a_1 column of the \mathbf{N} matrix, which are 2.0419. Solving the equation:

$$745 = \left(\frac{L}{A} \right) (2.0419) (2.574) \quad (3.51)$$

yields a value for $\frac{L}{A}$ of 141.75.

To keep the analysis as general as possible, this research assumes the outputs of the Hartmann sensor are the x- and y-tilts of each subaperture, in units of 514-nm wavelengths (*not* PMP units). Similar algebra yields a value for $\frac{L}{A}$ of 0.19025. The \mathbf{N} matrix derived in Appendix F should be premultiplied by this constant to get the \mathbf{H}' matrix used in Equations (3.39).

3.5.3 Derivation of \mathbf{R} The outputs of wavefront sensors are generally corrupted by noise. Numerous literature references [30:139] [14:30] [40:1772] [40:1773] [32:821] indicate the noise is zero-mean, white, Gaussian, uncorrelated from subaperture to subaperture, and uncorrelated to the wavefront phase. Possible sources of this noise include photon shot noise, A/D quantization noise (assuming the Hartmann outputs are digital), and thermal noise. The photon shot noise variance is inversely proportional to the number of photons counted during a measurement cycle [47]. The photon count is, in turn, related to light intensity. The lower the light intensity, the more shot noise there will be in the slope measurement. A/D quantization noise is typically uniformly distributed between minus 1/2 and plus 1/2 least significant bit. This distribution could be approximated as Gaussian with the $3\text{-}\sigma$ value set to 1/2 the least significant bit [24:364]. Thermal noise is related to absolute temperature, through Boltzman's constant.

Since the intensity of the viewed object is expected to vary greatly [23] as the target changes orientation with respect to the viewer, and also from target to target, it is likely that the shot noise contribution to the measurement noise will also vary. This research treats such noise as the dominant noise source, ignoring all others [47]. Therefore, this research includes a parameter study on the \mathbf{R} matrix. Using equations discussed in Welsh and Gardner [47], this research calculates slope noise strengths corresponding to 1000, 100, and 10 photons per subaperture. Table 3.2 shows values used for the diagonal elements of the \mathbf{R} matrix.

Table 3.2. Measurement Noise Strengths

| N | DESIGNATOR | R_{ii} (wavelength ²) |
|------|------------|-------------------------------------|
| 1000 | Low | 0.01755 |
| 100 | Medium | 0.0555 |
| 10 | High | 0.1755 |

3.6 Summary

This research develops stochastic models for atmospheric turbulence effects, deformable mirror dynamics, and a Hartmann-type wavefront sensor. The phase distortion due to atmospheric turbulence is modeled in the Zernike functional space. The Zernike coefficients are modeled as first-order Gauss-Markov random processes. The models are obtained by fitting theoretically-derived autocorrelation data to appropriate functions. Using data from the AFWL, this research synthesizes a deterministic dynamics model for a deformable mirror. The ability of the mirror to reconstruct the 14th Zernike function is verified in a simple simulation. The measurement matrix H is calculated by projecting each Zernike mode of distortion into subaperture slope space, incorporating an appropriate weighting function. Finally, values of slope sensor noise due to photon shot noise are calculated, to be used as a varying parameter in simulations.

IV. Controller Design

4.1 Kalman Filter Design

The Kalman filter for this research is of the same order as the truth model. Since both the atmosphere and the mirror Zernike coefficients are first-order processes, the Kalman filter is a 28-state filter—14 for the atmosphere and 14 for the mirror. For the time-invariant model assumed here, the continuous-time dynamics and discrete-time measurement truth model equations are:

$$\dot{\underline{x}}(t) = \underline{F}\underline{x}(t) + \underline{B}\underline{u}(t) + \underline{w}(t) \quad (4.1)$$

$$\underline{z}(t_i) = \underline{H}\underline{x}(t_i) + \underline{v}(t_i) \quad (4.2)$$

The \underline{F} and \underline{Q} matrices are diagonal, with elements given in Table 4.1. The y tilt and x-tilt noise strengths have been attenuated to reflect the presence of tilt mirrors. These tilt mirrors are modeled as removing 95 percent of atmosphere-induced tilt. The \underline{B} matrix is merely determined using Equations (3.35) and (3.37); the \underline{M} matrix is given in Appendix E. The \underline{H} matrix is determined from Equations (3.39), (3.50), and the \underline{N} matrix of Appendix F. The noise variance matrix, \underline{R} is an identity matrix premultiplied by one of the values of Table 3.2, depending on the noise model.

The filter models the continuous-time dynamics of the truth model in the discrete domain as suggested by Equation (2.38), forgoing on-line integration. Table 4.2 summarizes the dimensionality of the discrete state-space filter model for the adaptive optics system.

With a sample period of 7 milliseconds (the maximum sampling rate of the Reticon chip in the Hartmann sensor [27]), the state transition matrix for this time-invariant system model is calculated as [24:42]:

$$\Phi(t_{i+1} - t_i) = e^{(\underline{F})(0.007)} \quad (4.3)$$

Table 4.1. Continuous State-Space Model

| i | F_{ii} (second ⁻¹) | Q_{ii} (wavelength ² /second ²) |
|-----|----------------------------------|--|
| 1 | $-\frac{1}{0.07}$ | 0.1605 |
| 2 | $-\frac{1}{0.15}$ | 0.075 |
| 3 | $-\frac{1}{0.085}$ | 0.405 |
| 4 | $-\frac{1}{0.023}$ | 0.800 |
| 5 | $-\frac{1}{0.035}$ | 0.509 |
| 6 | $-\frac{1}{0.036}$ | 0.124 |
| 7 | $-\frac{1}{0.02}$ | 0.223 |
| 8 | $-\frac{1}{0.023}$ | 0.210 |
| 9 | $-\frac{1}{0.02}$ | 0.241 |
| 10 | $-\frac{1}{0.12}$ | 0.363 |
| 11 | $-\frac{1}{0.018}$ | 0.0694 |
| 12 | $-\frac{1}{0.015}$ | 0.0833 |
| 13 | $-\frac{1}{0.067}$ | 0.0645 |
| 14 | $-\frac{1}{0.015}$ | 0.117 |
| 15 | $-\frac{1}{0.00045}$ | 0 |
| 16 | $-\frac{1}{0.00045}$ | 0 |
| 17 | $-\frac{1}{0.00045}$ | 0 |
| 18 | $-\frac{1}{0.00045}$ | 0 |
| 19 | $-\frac{1}{0.00045}$ | 0 |
| 20 | $-\frac{1}{0.00045}$ | 0 |
| 21 | $-\frac{1}{0.00045}$ | 0 |
| 22 | $-\frac{1}{0.00045}$ | 0 |
| 23 | $-\frac{1}{0.00045}$ | 0 |
| 24 | $-\frac{1}{0.00045}$ | 0 |
| 25 | $-\frac{1}{0.00045}$ | 0 |
| 26 | $-\frac{1}{0.00045}$ | 0 |
| 27 | $-\frac{1}{0.00045}$ | 0 |
| 28 | $-\frac{1}{0.00045}$ | 0 |

Table 4.2. Dimensionality of Kalman Filter Vectors and Matrices

| Matrix/Vector | Dimension |
|----------------------|------------------|
| $\Phi(t_{i+1}, t_i)$ | 28×28 |
| $\underline{x}(t_i)$ | 28×1 |
| B_d | 28×97 |
| $\underline{u}(t_i)$ | 97×1 |
| $\underline{w}(t_i)$ | 28×1 |
| Q_d | 28×28 |
| $\underline{z}(t_i)$ | 138×1 |
| H | 138×28 |
| $\underline{v}(t_i)$ | 138×1 |
| R | 138×138 |

Since F is a diagonal matrix, so is $\Phi(t_{i+1} - t_i)$, and the exponentiation is easily accomplished term-by-term. The discrete version of the dynamics driving noise is determined using Equation (2.39). For this time-invariant model, with G being the identity matrix, and F being diagonal, Equation (2.39) is manipulated:

$$\begin{aligned}
 Q_d &= \int_{t_i}^{t_{i+1}} \Phi(t_{i+1} - \tau) G Q G^T \Phi^T(t_{i+1} - \tau) d\tau \\
 &= \int_0^{0.007} e^{F(0.007-\tau)} Q e^{F(0.007-\tau)} d\tau \\
 &= Q \int_0^{0.007} e^{2F(0.007-\tau)} d\tau \\
 &= Q e^{2F \cdot 0.007} \int_0^{0.007} e^{-2F\tau} d\tau \\
 &= Q e^{2F \cdot 0.007} \left[e^{-2F\tau} \frac{-F^{-1}}{2} \right]_0^{0.007} \\
 &= Q e^{2F \cdot 0.007} \left[e^{-2F \cdot 0.007} - I \right] \left[\frac{-1}{2} F^{-1} \right] \\
 &= \frac{1}{2} Q F^{-1} \left[I - e^{-2F \cdot 0.007} \right]
 \end{aligned} \tag{4.4}$$

The diagonal elements of $\Phi(t_{i+1}-t_i)$ and Q_d are given in Table 4.3. Non-diagonal elements are zero.

The Kalman filter processes the 138 slope measurements every 0.007 seconds using Equations (2.43) through (2.47). The filter assumes the measurements are available instantly. The important output of the filter is the estimate of the system state, since this is ultimately multiplied by the controller gain.

The Kalman filter requires initial conditions on both the state estimate $\hat{\mathbf{x}}(0)$ and covariance $\mathbf{P}(0)$. Since the states model the Zernike coefficients as zero-mean, the initial filter estimate of the system state is selected to be a zero vector. The first 14 diagonal elements of $\mathbf{P}(0)$ are set to large values to reflect initial uncertainty.

4.2 Linear Quadratic Regulator Design

Equation (2.41) defines the cost to be minimized by the quadratic regulator. For the adaptive optics system of interest, it makes sense to assign cost to the phase distortion in the reflected image, since this is the image which is desired to be distortionless. It also makes sense to assign cost to the control voltages, since they are restricted to be within a finite range (± 10 volts). The derivation of both the \mathbf{X} and the \mathbf{U} cost matrices are now discussed.

The phase distortion in the reflected image is modeled by its set of Zernike coefficients. This set of Zernike coefficients is obtainable from the discrete state vector by:

$$\begin{bmatrix} \mathbf{A} & | & \mathbf{I} \end{bmatrix} \begin{bmatrix} \mathbf{x}_a(t_i) \\ - - - \\ \mathbf{x}_m(t_i) \end{bmatrix} \quad (4.5)$$

The quadratic cost associated with the distortion in the reflected image is:

$$\left(\begin{bmatrix} \mathbf{A} & | & \mathbf{I} \end{bmatrix} \begin{bmatrix} \mathbf{x}_a(t_i) \\ - - - \\ \mathbf{x}_m(t_i) \end{bmatrix} \right)^T \mathbf{C} \left(\begin{bmatrix} \mathbf{A} & | & \mathbf{I} \end{bmatrix} \begin{bmatrix} \mathbf{x}_a(t_i) \\ - - - \\ \mathbf{x}_m(t_i) \end{bmatrix} \right) \quad (4.6)$$

Table 4.3. Filter State Transition Matrix and Discrete Driving Noise

| j | $\Phi_{jj}(t_{i+1}, t_i)$ | Q_{djj} (wavelength ²) |
|-----|---------------------------|--------------------------------------|
| 1 | 0.904810273562201 | 0.004073001858519 |
| 2 | 0.954383210022565 | 0.002004933000163 |
| 3 | 0.920977197358095 | 0.010455681053018 |
| 4 | 0.737595286709826 | 0.016778406543654 |
| 5 | 0.818738942175464 | 0.011746606438655 |
| 6 | 0.823279104805153 | 0.002876474222156 |
| 7 | 0.704688089718714 | 0.004490459090181 |
| 8 | 0.737595286709826 | 0.004404331717709 |
| 9 | 0.704688089718714 | 0.004852917671451 |
| 10 | 0.943357461794596 | 0.009593719616645 |
| 11 | 0.677788484408774 | 0.001350533885479 |
| 12 | 0.627118334037179 | 0.001516351317027 |
| 13 | 0.960765787779704 | 0.001629746010087 |
| 14 | 0.627074461402559 | 0.002129683020039 |
| 15 | 0.000000175785735 | 0.000000000000000 |
| 16 | 0.000000175785735 | 0.000000000000000 |
| 17 | 0.000000175785735 | 0.000000000000000 |
| 18 | 0.000000175785735 | 0.000000000000000 |
| 19 | 0.000000175785735 | 0.000000000000000 |
| 20 | 0.000000175785735 | 0.000000000000000 |
| 21 | 0.000000175785735 | 0.000000000000000 |
| 22 | 0.000000175785735 | 0.000000000000000 |
| 23 | 0.000000175785735 | 0.000000000000000 |
| 24 | 0.000000175785735 | 0.000000000000000 |
| 25 | 0.000000175785735 | 0.000000000000000 |
| 26 | 0.000000175785735 | 0.000000000000000 |
| 27 | 0.000000175785735 | 0.000000000000000 |
| 28 | 0.000000175785735 | 0.000000000000000 |

where the C is a diagonal matrix of cost elements. Assume one desires the maximum rms phase deviation due to any Zernike mode to be $1/20$ of a wavelength. Remembering that the Zernike coefficients map directly into rms phase distortion, one can say the maximum value for any Zernike coefficient is $1/20$. Each diagonal term of C , for the first design, can be set equal to the reciprocal of the square of the maximum value [25:69]. Therefore, the diagonal elements of C are 400, with all other elements zero, for initial tuning.

Manipulating the expression in Equation (4.6) one obtains:

$$\begin{bmatrix} \underline{x}_a^T(t_i) & \underline{x}_m^T(t_i) \end{bmatrix} \begin{bmatrix} A^T C A & A^T C \\ C A & C \end{bmatrix} \begin{bmatrix} \underline{x}_a(t_i) \\ \underline{x}_m(t_i) \end{bmatrix} \quad (4.7)$$

which is exactly of the form

$$\underline{x}^T X \underline{x} \quad (4.8)$$

The extraction matrix A is a 14-by-14 identity matrix for this research, since each atmospheric Zernike coefficient is modeled as first-order Gauss-Markov. Therefore, the state cost matrix X is a 28-by-28, singular, banded diagonal matrix:

$$X = \begin{bmatrix} C & C \\ C & C \end{bmatrix} \quad (4.9)$$

The first design iteration of the cost matrix U associated with the control voltages is simpler to derive. The maximum allowed control voltage to any actuator is ± 10 volts. Using the reciprocal-squared method results in the initial design for the U matrix being a diagonal matrix with diagonal elements of 0.01. If the simulated performance of the adaptive optics system is unacceptable, these cost matrices can be varied to try to improve performance.

Knowing the $\Phi(t_{i+1}-t_i)$, B_d , X , and U matrices, one can use the Martix-X command "DREGULATOR" to obtain the steady-state solution of the backward Riccati equation and obtain the optimal steady-state controller gain matrix G_c^* (See Equations (2.51) and (2.52)). This value of G_c^* can now be used as the controller gain in a digital simulation of the adaptive optics system. The cost matrices X and U can be adjusted to try to

improve performance. The controller multiplies its optimal gain by the state estimate from the Kalman filter to obtain a set of control voltages for the mirror actuators (See Equation (2.50)).

4.3 Summary

This chapter assembles the results of previous chapters into suitable Kalman filter and controller form. The cost matrices X and U are calculated for the first iteration of controller design. Matrix-X software is used to solve for the steady-state controller gain. Depending on simulation results, the cost matrices may need to be tuned to maximize performance, i.e., minimize rms phase distortion in the reflected image.

V. Simulation Results

5.1 Methodology

A digital simulation of the adaptive optics system was desired in order to test the effectiveness of the LQG controller in reducing phase aberration. The Multimode Simulation for Optimal Filter Evaluation (MSOFE) software tool was used [28]. The simulation involved implementing a truth model of the atmosphere/mirror/sensor system to generate simulated discrete-time Hartmann sensor measurements. The Kalman filter, also embedded in the simulation, processed these simulated measurements and determined the estimate of the 28 truth model states. The LQ regulator then multiplied this state vector estimate by the optimal controller gain (pre-calculated off-line), and the resulting control voltage commands were sent to the simulated mirror actuators. The nonlinearity of the mirror response to applied control voltage was simulated by limiting the mirror voltage to the ± 10 volt region. For example, if the controller tried to command an 11-volt control voltage to an actuator, logic in the simulation program truncated the value to 10 volts. This nonlinearity imposed the use of multiple Monte Carlo simulations, as opposed to a single covariance analysis [24:329] [28].

Output from the simulation included time histories of the 28 truth-model states, the filter's estimates of these states, the filter covariance matrices, and the maximum and minimum control voltages of the mirror actuators. Post-simulation data reduction yielded time histories of the rms phase distortion at the optics entrance aperture as well as the rms phase distortion after correction. The Matrix-X software package was used to perform the data reduction as well as generate plots of time histories. In addition to single realizations of these time histories, ensemble statistics were generated using Monte Carlo analysis of ten runs.

As previously discussed, there is expected to be significant variation of measurement noise strength, i.e., the elements of the \mathbf{R} matrix, in a real adaptive optics system. The simulation was performed in nine "studies" in order to investigate performance sensitivity to \mathbf{R} . Each study simulated a different combination of truth model and filter model measurement noise strengths. Table 5.1 shows the combinations simulated.

Table 5.1. Truth and Filter Model Measurement Noise Strengths

| STUDY | TRUTH | FILTER |
|-------|--------|--------|
| 1 | Low | Low |
| 2 | Medium | Medium |
| 3 | High | High |
| 4 | Low | Med |
| 5 | Low | High |
| 6 | Medium | Low |
| 7 | Medium | High |
| 8 | High | Low |
| 9 | High | Medium |

The noise strengths of "Low", "Medium", and "High" correspond to photon counts per subaperture of 1000, 100, and 10, respectively; see Table 3.2. The objective here was to determine the effect of mismodeling the noise strength in the Kalman filter. In a real implementation, R in the filter model may be fixed and therefore wrong for the case of the true, intensity-dependent measurement noise. Since the regulator design was based on a deterministic version of the stochastic dynamic equations due to certainty equivalence, changing the R matrix does not affect the steady-state value of the regulator gain matrix G_c^* . Thus, all nine studies used the same regulator gain matrix. The following discussion presents a verbal and graphical description of study 1.

5.2 Study 1 Description

Study 1, having low measurement noise correctly modeled in the Kalman filter, is the most optimistic of the studies from a performance perspective. Since the mirror (states 15-28) is assumed deterministic in both the truth and filter models, the filter estimates of the mirror states are trivial, and they will be omitted from most of the discussion. In an operational system these deterministic states should not even be included in the Kalman filter, for computational reasons. Their inclusion in the filter here is merely convenient.

5.2.1 Simulated Atmospheric State Behavior This research models image phase distortion induced by atmospheric turbulence as fourteen time-varying Zernike coefficients. It is arbitrarily assumed that tilt mirrors ahead of the adaptive optics system remove 95 percent of the first two Zernike modes (y-tilt and x-tilt). Zernike coefficients for the remaining tilt distortion as well as the other twelve modes are states 1-14 of the truth model. Figure 5.1 shows a time-history of a sample realization of the y-tilt Zernike coefficient x_1 as well as the filter estimate, \hat{x}_1 .

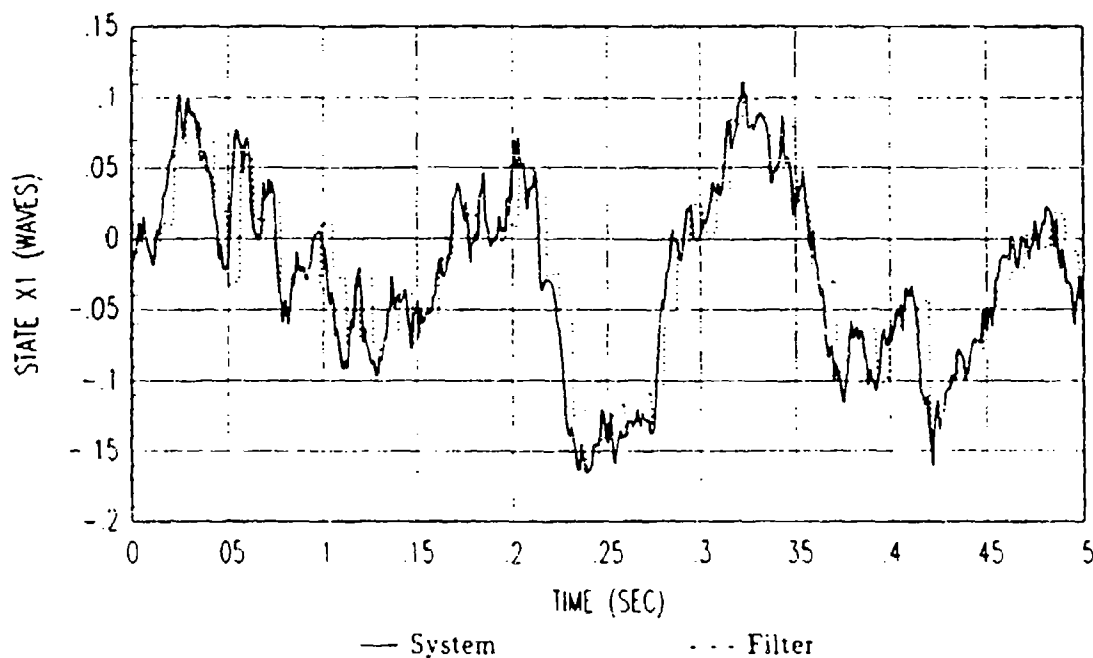


Figure 5.1. Atmospheric Y-tilt State and Filter Estimate

Filter error can be defined as the true state minus the filter estimate of the state. The filter covariance P is the filter's indication of uncertainty in its estimates, as in Equation (2.42). The square root of the (1,1) element of the P matrix is what the filter believes to be the $1-\sigma$ value of its error. Although Figure 5.1 shows that the filter appears to be tracking the true state value, it does not indicate how the actual filter error compares with

what it thinks are its 1- σ values. Figure 5.2 shows a time history of the filter error for state 1, as well as these filter-computed 1- σ values.

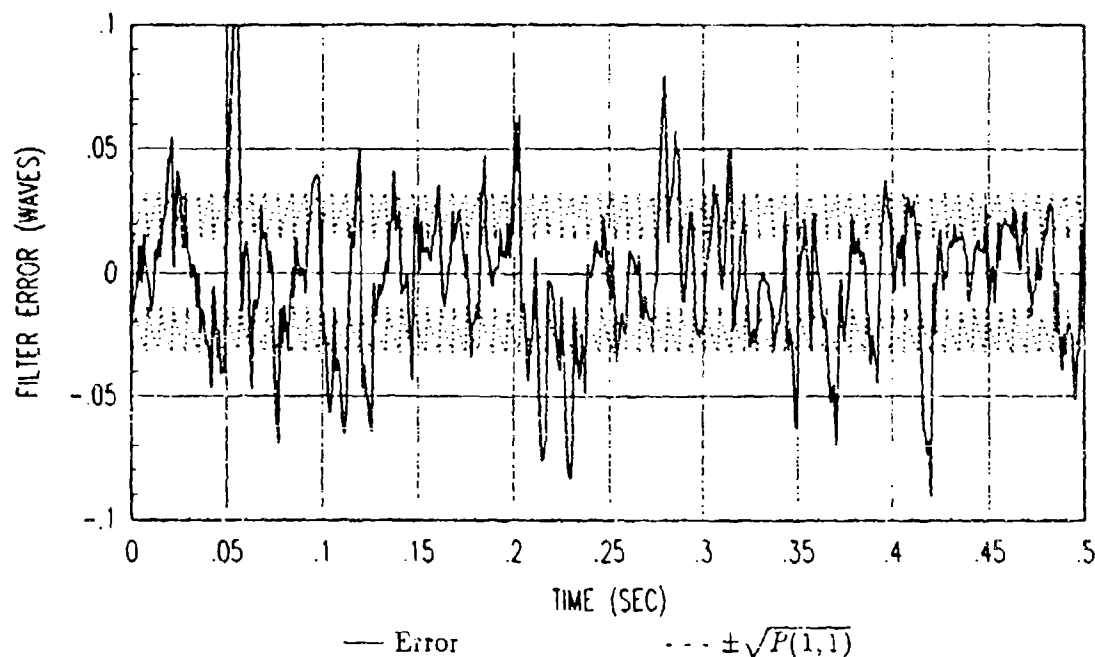


Figure 5.2. Atmospheric Y-tilt Filter Error and Filter Variance

Looking at the single-sample realization of filter error of Figure 5.2 and assuming the error is an ergodic random process, it appears that $\pm\sqrt{P(1,1)}$ is a reasonable 1- σ value for the error, and that the error is zero mean. In order to obtain the "true" error mean and variance, a Monte Carlo analysis of ten runs was accomplished. The equations used to process the results of these ten runs are:

$$\mu_E(t) \approx \frac{1}{10} \sum_{k=1}^{10} e_k(t) \quad (5.1)$$

$$\sigma_E^2(t) \approx \frac{1}{10-1} \sum_{k=1}^{10} [e_k^2(t) - \mu_E^2(t)] \quad (5.2)$$

where

$$\begin{aligned} e_k(t) &= x_k(t) - \hat{x}_k(t) \text{ (wavelengths)} \\ k &= \text{sample realization number} \\ \mu_E(t) &= \text{mean of random process } E(t) \text{ (wavelengths)} \\ \sigma_E^2(t) &= \text{variance of random process } E(t) \text{ (wavelengths}^2\text{)} \end{aligned}$$

Figure 5.3 shows a plot of the mean and standard deviation of the filter error for state 1, as calculated from the ten sample realizations using Equations (5.1) and (5.2). Visual inspection of this plot reveals the error process is approximately zero mean, with standard deviations approximately equal to the $\sqrt{P(1,1)}$ values from Figure 5.2. If more sample realizations had been included in the Monte Carlo analysis, the similarity would most likely be even greater.

Plots similar to those of Figures 5.1, 5.2, and 5.3, can be found in Appendix G for the remaining 13 states corresponding to image phase distortion prior to correction. This complete set of plots is for study 1 only.

5.2.2 Performance Analysis The performance of the LQG controller can be expressed in terms of rms phase distortion in the corrected image versus the rms phase distortion of the incident image. Again, incident here means after the tilt mirrors have removed most of the gross tilt. States 1—14 of the system model are the Zernike coefficients for atmosphere-induced phase distortion, and states 15—28 are Zernike coefficients for the mirror-induced "counterdistortion". Since reflection from the deformable mirror is modeled as addition of atmospheric and mirror phase distortions, the Zernike coefficients of the reflected (i.e., corrected) image are:

$$\underline{a}(t) = \underline{a}_a(t) + \underline{a}_m(t) \quad (5.3)$$

$$= \underline{x}_{1-14}(t) + \underline{x}_{15-28}(t) \quad (5.4)$$

$$= [\mathbf{I} \mid \mathbf{I}] \underline{x}(t) \quad (5.5)$$

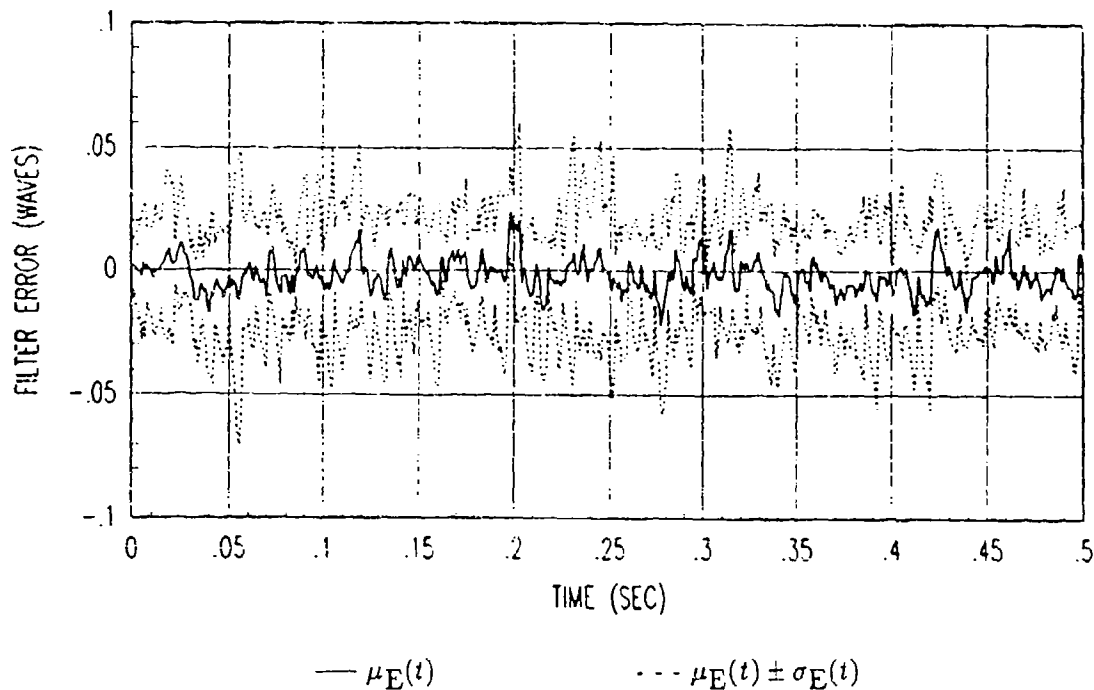


Figure 5.3. Mean and Standard Deviation of Atmospheric Y-tilt Filter Error

It has already been shown that the rms phase distortion is the square root of the sum of the squares of the Zernike coefficients (see Appendix C). The rms phase error of the incident image is:

$$\phi_{rms}(t) = \sqrt{\sum_{i=1}^{14} (x_i)^2} \quad (5.6)$$

and for the corrected image, the rms phase distortion is:

$$\phi_{rms}(t) = \sqrt{\sum_{i=1}^{14} (x_i + x_{i+14})^2} \quad (5.7)$$

A time history of a sample realization of the rms phase distortion is shown in Figure 5.4 for both the incident and corrected images. The values for this plot were obtained during the post-simulation data reduction phase of the study, using Equations (5.6) and (5.7).

The plot clearly shows the reduction in rms phase error. Moreover, this single realization shows the rms phase error of the corrected image tends to stay in the vicinity of about 0.1 wavelength, whereas the rms phase error of the incident image varies between about 0.1 wavelength and 0.5 wavelength.

Calculating similar results for each of the ten Monte Carlo realizations and generating the usual statistics results in values plotted in Figure 5.5. The upper three lines of the graph show the mean and the $[\text{mean} \pm 1-\sigma]$ values on the rms phase distortion of the incident image. The apparent transient in these three lines during the initial 0.05 seconds of the simulation was caused by unrealistic initial conditions in the truth model (all states zero). It would be a more realistic simulation if the initial true states were random. The lower three lines of the graph represent the mean and the $[\text{mean} \pm 1-\sigma]$ values on the rms phase distortion of the corrected image. One feature of note is that the $1-\sigma$ values on the corrected image are tighter than on the incident image. This seems to suggest the quality of the corrected image is somewhat constant, despite wide variation in the amount of atmospheric distortion. Another feature is the sawtooth appearance of the lower set of plots. The period of the sawtooth appears to be the Hartmann sampling period (0.007 sec). This suggests the correction is most effective just after a measurement, and degrades as the atmosphere changes between measurements. One may wonder if even better performance is possible. In other words, one can ask, what is limiting the performance shown in Figure 5.5? At least three answers are possible: 1) saturation of mirror actuators, 2) improperly chosen weighting matrices in the LQ regulator, or 3) the filter's estimation errors. The first possible reason, actuator saturation, is immediately eliminated based on Figure 5.6. This plot shows the absolute envelope for the actuator control voltages for the ensemble of ten Monte Carlo realizations. Given that saturation occurs when the magnitude of the commanded voltage exceeds 10 volts, and the maximum actual excursion was only about \pm one volt, saturation did not occur. In fact, one could say the mirror had quite a bit of "remaining" capability left. The second reason, improperly chosen weighting matrices X and U , was eliminated by a tuning experiment. The nonzero elements of the X

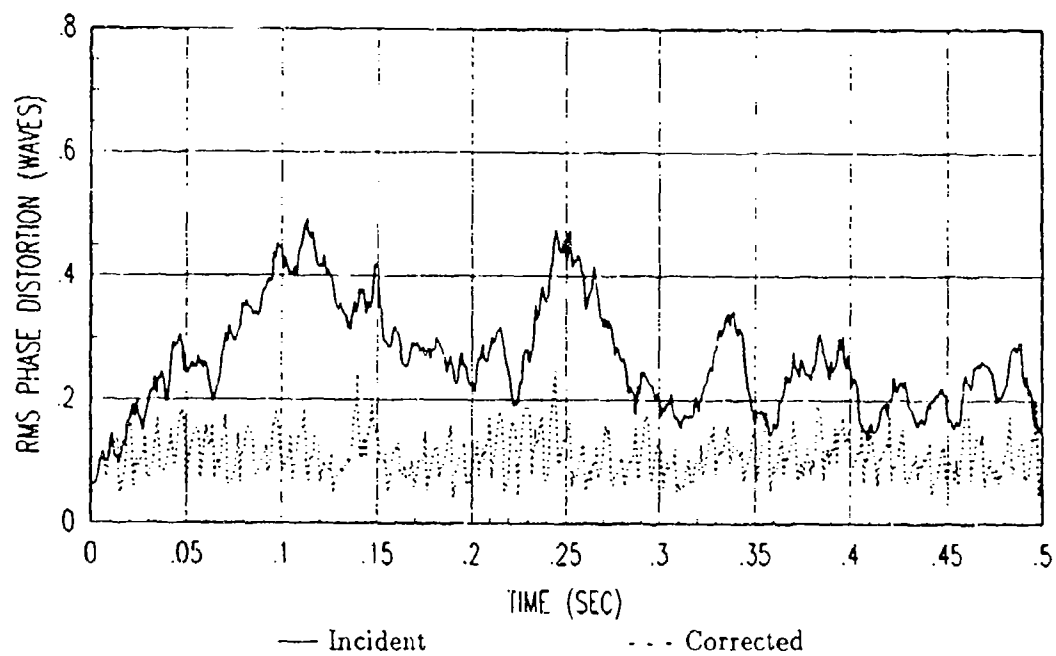


Figure 5.4. RMS Phase Distortion Before and After Correction

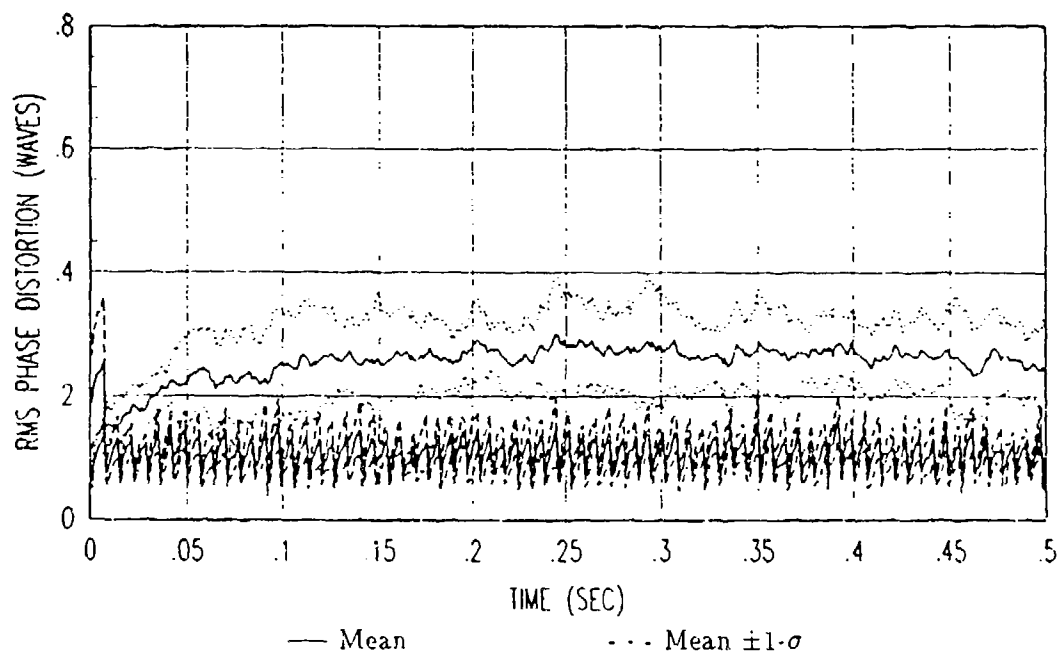


Figure 5.5. Monte Carlo Study of RMS Phase Distortion Before and After Correction

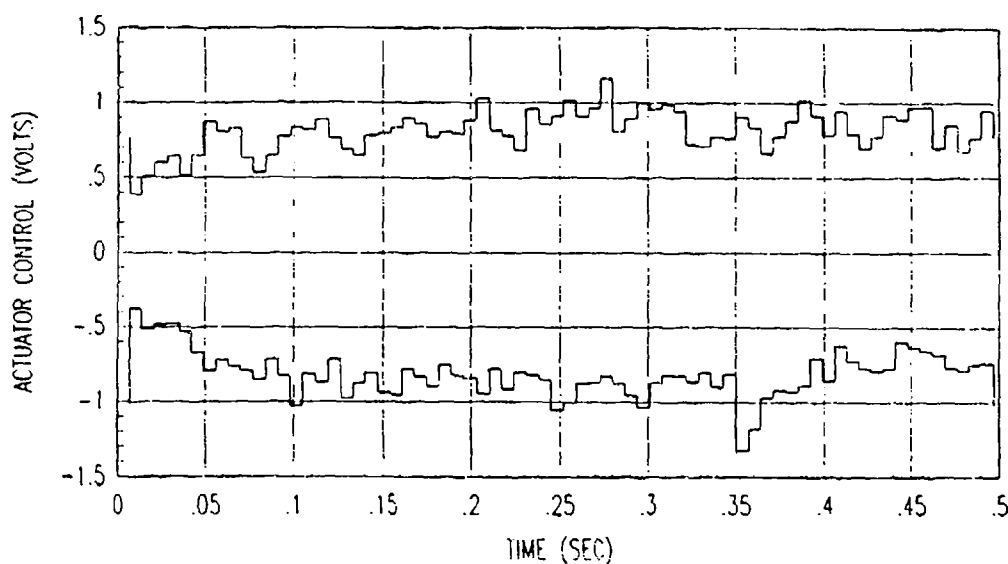


Figure 5.6. Control Voltage Envelope for Monte Carlo Study

matrix of the cost equation were increased by 50 percent. This penalized the distortion of the corrected image more heavily. The simulation was re-run using the new steady-state controller gain, G_c^* , and performance did not improve. The third reason, filter estimation error, was analyzed in the following manner. The filter's function is essentially to estimate the Zernike coefficients of the incident, uncorrected image. Assume the regulator/mirror combination can perfectly implement the filter's estimate (without a sign change). The rms phase error due *solely to the filter's estimation error* can be thought of as the lower bound on rms phase error attainable and is calculated using:

$$\phi_{rms}(t) = \sqrt{\sum_{i=1}^{14} (x_i - \hat{x}_i)^2} \quad (5.8)$$

Monte Carlo analysis of values calculated using Equation (5.8) is shown in Figure 5.7. The extreme similarity of this graph and the lower three plots of Figure 5.5 strongly suggest that filter estimation error is the performance-limiting factor. An alternate method of

determining the contribution of filter estimation error to the rms phase distortion would be to input \underline{x} instead of $\hat{\underline{x}}$ into the controller, and see if the rms error is eliminated. This alternate method was not used in this research.

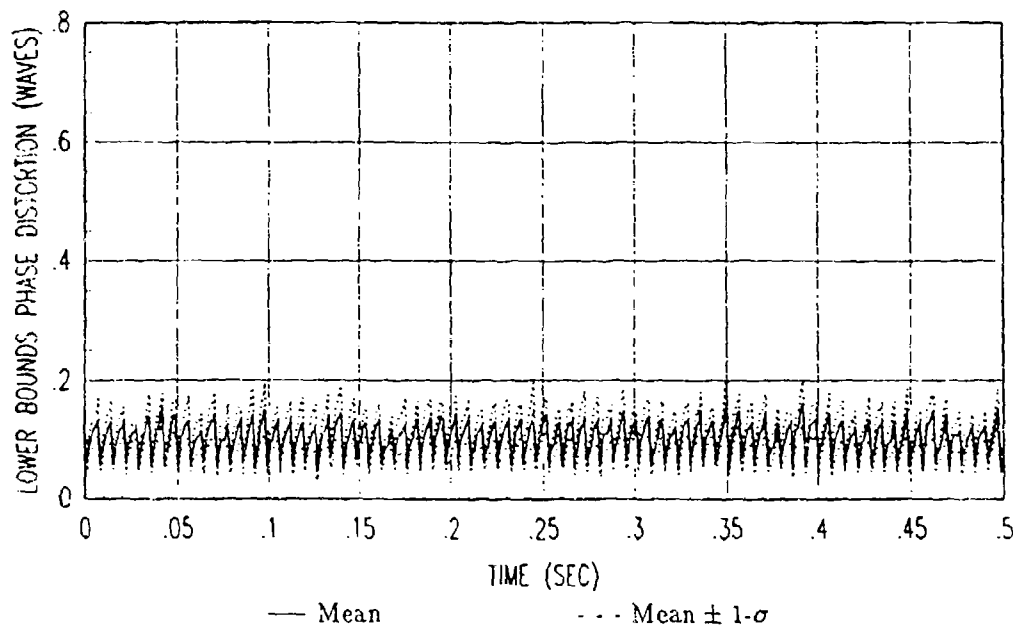


Figure 5.7. Monte Carlo Study of RMS Phase Distortion Caused by Filter Error

5.3 Performance Results

The above analysis section dealt exclusively with study 1, the case of low measurement noise correctly modeled in the filter. Similar graphs for the remaining eight Studies are shown in Appendix H. (Also shown are filter estimation plots for Zernike modes 1 and 14.) In order to compare results from the nine studies conveniently, further data compression was accomplished. This amounted to time-averaging the mean-value plots of rms phase distortion from each of the nine Monte Carlo studies. Thus each of the nine studies is summarized by three numbers: the rms phase distortion of the incident image,

the rms phase distortion of the corrected image, and the rms phase distortion which could be achieved if the regulator/mirror could perfectly implement the filter's estimate, i.e., the filter "error." Furthermore, all three of these numbers can be normalized by dividing by the first. This normalization provides a fairer comparison across the nine studies. Table 5.2 shows the results of this time-averaging and normalization.

Table 5.2. Summary of Adaptive Optics System Simulated Performance

| STUDY | RMS DISTORTION | | | NORMALIZED | | |
|-------|----------------|--------|--------|------------|--------|--------|
| | Inc. | Cor. | Flt. | Inc. | Cor. | Flt. |
| 1 | 0.2552 | 0.1083 | 0.1031 | 1 | 0.4244 | 0.4040 |
| 2 | 0.2557 | 0.1126 | 0.1079 | 1 | 0.4404 | 0.4220 |
| 3 | 0.2598 | 0.1321 | 0.1285 | 1 | 0.5085 | 0.4946 |
| 4 | 0.2546 | 0.1088 | 0.1033 | 1 | 0.4273 | 0.4057 |
| 5 | 0.2536 | 0.1187 | 0.1112 | 1 | 0.4681 | 0.4385 |
| 6 | 0.2543 | 0.1124 | 0.1081 | 1 | 0.4420 | 0.4251 |
| 7 | 0.2565 | 0.1201 | 0.1131 | 1 | 0.4682 | 0.4409 |
| 8 | 0.2511 | 0.1428 | 0.1446 | 1 | 0.5687 | 0.5759 |
| 9 | 0.2478 | 0.1356 | 0.1362 | 1 | 0.5472 | 0.5496 |

Inc. = Incident Image

Cor. = Corrected Image

Flt. = Filter Error

As expected, study 1 resulted in the lowest rms phase distortion in the corrected image. This was the case of low measurement noise, correctly modeled in the filter. That the rms phase distortion of the corrected image was only slightly larger than the rms phase error caused by the filter error indicates that most of the phase error in the corrected image was due to filter estimation errors. As the true measurement noise increased (studies 1 \rightarrow 2 \rightarrow 3), and the filter \mathbf{R} was modified correspondingly, the performance was progressively poorer. This reflects the fact that noisier measurements resulted in a less accurate state estimation, even with the filter properly tuned.

The worst performance came from study 8. This was the case of high measurement

noise, mismodeled in the filter as low measurement noise. Heuristically, the filter had too much confidence in the incoming measurements, and tended to disregard it's own model of the dynamics. The result was a corrected image having an rms phase distortion of 0.1428 wavelengths.

5.4 Summary

This chapter discusses the digital simulation of the adaptive optics system. The MSOFE software [28] is used to accomplish the simulation. This software simulates both real-world behavior and Kalman filter processing. Modifications to the software allow for implementation of LQG control. The simulations comprise a set of nine studies, each having a different combination of true measurement noise and filter model thereof. Study 1, the case of low measurement noise correctly modeled in the filter, is analyzed in detail. A table of results is presented which indicates filter estimation errors limit the controller's performance.

VI. Conclusions and Recommendations

6.1 Summary

This research considered the design of a nominal linear quadratic Gaussian (LQG) controller for a ground-based adaptive-optics telescope. Phase distortion caused by atmospheric turbulence was modeled as 14 time-varying Zernike coefficients. The effect of tilt mirrors was modeled as removing 95 percent of the mean square contribution of the first two Zernike modes. Dynamics of the 97-actuator deformable mirror, following the tilt mirrors in the optical path, were modeled as a 14 deterministic first-order lags.

A 69-subaperture Hartmann-type wavefront sensor was assumed to be the measurement device. The slope outputs from the subapertures comprised a 138-element measurement vector. The sampling period was assumed to be 7 milliseconds, corresponding to the maximum detector rate. A 28-state Kalman filter processed the measurements from the wavefront sensor and obtained estimates of system states. A constant-gain linear quadratic (LQ) regulator processed these state estimates and determined an appropriate set of commands for the deformable mirror.

The entire control system was digitally simulated using the Multimode Simulation for Optimal Filter Evaluation (MSOFE) software. Nine simulation studies were conducted to investigate the effects of mismodeling the noise in the measurement device.

6.2 Conclusions

1. The LQG approach used in this research makes sense because the desired goal of reducing the rms phase error translates directly into the quadratic cost criteria. The mean-square phase distortion is the sum of the squares of the Zernike coefficients (states).
2. Most of the open literature models atmospheric turbulence as having Kolmogorov properties. Taylor's frozen field assumption is also popular. Results based on actual *measurements* of atmospheric effects on image quality are sparse.

3. Assuming the atmospheric distortion is well-modeled by the Gauss-Markov processes of this research, the deformable mirror operates in the linear region, i.e., its actuators are seeing control voltages in the ± 1 volt range, whereas saturation occurs at the ± 10 volt limits.
4. Modifications to the MSOFE software allowed for simulation of LQG control. These consisted of pre-multiplication of the filter state estimate vector (after measurement update) by the steady-state controller gain, pre-multiplication of this result by the input distribution matrix, and adding the result to the right-hand side of the dynamics equation.
5. Based on Monte Carlo simulation results, the adaptive optics system did reduce phase distortion in all cases. Table 5.2 shows that the (simulated) deformable mirror reduces the rms phase distortion to about 40—60 percent of its incident (post-tilt mirror) value. The best performance was achieved when the filter model of the measurement noise was "correct" relative to the truth model. When the measurement noise in the truth model increased, the performance degraded, even if the filter was retuned correspondingly.
6. A single realization of the performance history (Figure 5.4) hints that the phase quality of the corrected image is somewhat constant, regardless of the actual magnitude of the incoming atmospheric phase distortion. This result is most likely related to the operation of the actuators far from their saturation limits.
7. Comparison of the remaining phase distortion after correction to the phase distortion caused by filter estimation error (Figures 5.5 and 5.7) indicates that state estimation error is the factor most limiting performance.

6.5 Recommendations

6.5.1 Modeling This research is based on a set of nominal models, mostly derived from theoretical results. The aforementioned "performance" of the LQG control law is only as valid as the truth model of the real world. This research never claimed to develop